Controlled assembly of heterogeneous aggregates of clay, iron hydr(oxydes) and polysaccharide

Erwin A. Henry, Emmanuelle Montargès-Pelletier, Isabelle Bihannic, Céline Caillet, Jaafar Ghanbaja, Renaud Gley, Yves Waldvogel, Jérôme F.L. Duval

Controlled assembly of heterogeneous aggregates of clay, iron hydr(oxydes) and polysaccharide: effects of preparation conditions.

Erwin A. Henry[a,c], Emmanuelle Montarges-Pelletier[a,c,1], Isabelle Bihannic[a], Céline Caillet[a], Jaafar Ghanbaja[b], Renaud Gley[a], Yves Waldvogel[a], Jérôme F.L. Duval[a]

a. LIEC, Université de Lorraine CNRS, UMR 7360 15 avenue du Charmois 54500, Vandoeuvre lès Nancy, France ;
b. IJL, Université de Lorraine CNRS, UMR 7198, 2 allée André Guinier 54011, Nancy, France ;
c. LTSER Moselle, 54500, Vandoeuvre lès Nancy, France

[1] Corresponding author: E. Montarges-Pelletier, emmanuelle.montarges@univ-lorraine.fr

Abstract

The preparation of well-defined organo-mineral assemblies under controlled conditions is required to improve our understanding of the formation and surface reactivity of micrometric aggregates, ubiquitous in soils and continental aquatic media. We aim at investigating the building of organo-mineral assemblies with a specific focus on the assembly mode and its consequence on the final properties of the micrometric aggregates. In this work, the preparation and detailed characterization of clay-size aggregates composed of a clay mineral (illite), organic polymer (Dextran polysaccharide) and iron (hydr)oxide are reported, with a focus on the structural organisation of the generated aggregates. A step-by-step strategy was developed, and three sets of clay-size composites were prepared with illite particles as a starting material. In two first steps, two distinct sets of two-component composites were obtained according to different procedures. Illite-iron (hydr)oxide composites were obtained by alkaline hydrolysis of iron in the presence of illite particles, and illite-Dextran aggregates were obtained through the addition of Dextran polysaccharide to an illite suspension. In a third step, three-component micro-aggregates were obtained by subsequent addition of Dextran to suspensions containing the formed illite-iron (hydr)oxide composite. The so-prepared 2- and 3- component aggregates were investigated by electrophoresis, electron microscopy, X-ray absorption and FTIR spectroscopies. For materials containing Dextran, electrophoretic mobility measurements evidenced variations of surface charge, combined with an increase of aggregate size highlighted by dynamic light scattering. Electron microscopy and EXAFS at iron K-edge evidenced the precipitation of nanoparticles of iron (hydr)oxide onto clay mineral surfaces. FTIR data in transmission and diffuse reflectance modes supported not only the adsorption of Dextran but also the preferential localization of Dextran at the external surfaces of the aggregates. All in all, data collected on the two- and three-component materials demonstrated that the presence of iron (hydr)oxide nanoparticles on the surface of illite strongly modified the organization of organic and mineral constituents.

1. Introduction

Colloids and microparticles are ubiquitous in natural systems, soils and surface waters, and play a key role in the contaminant dynamics (organic, metallic and/or biological) through e.g. adsorption phenomena (Warren and Zimmermann, 1994; Buffle et al., 1998; Mavrocordatos et al., 2007; Wilkinson and Lead, 2007; Walling, 2013; Vindedahl et al., 2016). Those natural entities display a multiphasic character, with organic, mineral and biological components whose organization and spatial distribution obviously affect their surface properties (Mavrocordatos et al., 2007; Vindedahl et al., 2016). The physico-chemical and adsorption properties of the building units composing environmental particles, such as clay minerals, iron (hydr)oxides or humics, have been investigated extensively (Rey-Castro et al., 2009; Tertre et al., 2009; Churakov and Dähn, 2012). Whereas this abundant literature is of major interest for the understanding and prediction of e.g., contaminant behaviour, there remains a true need for addressing how complexity and heterogeneity of these clay-size composites affect their reactivity compared to those inferred from separate consideration of components contribution. Several

publications report the study of clay-composites (Nachtegaal and Sparks, 2004; Sipos et al., 2008, 2018; Moon and Peacock, 2012; Du et al., 2016, 2018; Sowers et al., 2018a) but information is missing about the way the different constituents are organized within the clay-size aggregates, which prevents the firm drawing of mechanistic conclusions on reactivity features. A condition for deriving generic information on the relationship between reactivity and heterogeneity of composite organo-mineral particles is, first, to have at disposal well-defined organo-mineral assemblies whose structure and composition are fully addressed from the molecular to colloidal scale.

Accordingly, we aim at building clay-size aggregates and investigating the influence of the preparation mode on their external properties. Thus, we report below the preparation and characterization of two-component and three-component aggregates with two minerals (illite and iron (hydr)oxide) and one organic constituent (polysaccharide). Those assemblies will be referred to as binary or ternary aggregates depending on the number of components used to prepare them. The selection of these building components is motivated by the predominance of illite particles in the clay mineralogy of river SPM (Le Meur, 2016; Le Meur et al., 2017), the targeted natural particles. Iron (hydr)oxide coatings were commonly reported in soil micro-aggregates (Goldberg, 1989; Colombo and Torrent, 1991; Kleber et al., 2007; Totsche et al., 2018; Gao et al., 2020; Krause et al., 2020) and were also evidenced in river suspended particulate matter (SPM) (Le Meur, 2016). Those poorly crystalline iron (hydr)oxides are known to play a crucial role in the formation of micro-aggregates, as cementing agents (Totsche et al. 2018) and also in the interactions between mineral and organic constituents in soils (Vindedahl et al., 2016; Sowers et al., 2018a; Adhikari et al., 2019). Accordingly, to build mineral assemblies that most adequately reflect the complex physicochemical composition of natural river particles, we considered iron (hydr)oxide as a component to be included in our model aggregates. Recalling that iron (hydr)oxide is supposedly poorly crystalline under natural conditions, pure iron oxide and iron hydr(oxide) minerals such as goethite, lepidocrocite or ferrihydrite were not considered. Instead, the “addition of iron (hydr)oxide” step in our synthesis protocol was performed as a controlled precipitation of iron (hydr)oxide in the presence of illite particles, thereby enhancing the precipitation reaction rate due to the overall surface area of dispersed illite particles. The preparation of illite-iron (hydr)oxide composites was based on the hydrolysis of iron salt in the presence of illite particles with or without late addition of organic polymer. Numerous studies reported the precipitation of ferrihydrite or ferrihydrite precursors in the presence of different salts and/or different ligands, with cation substitution (Mikutta and Kretzschmar, 2008; Cismasu et al., 2012, 2014; Hofmann et al., 2013; Guénet et al., 2017; Adhikari et al., 2019; Beauvois et al., 2020) or in the presence of montmorillonite (Green-Pedersen and Pind, 2000; Yuan et al., 2008; Borgnino et al., 2009). To favour the formation of nanoparticulate iron (hydr)oxides, closely associated to the clay minerals, relatively low concentrations of iron were used. The efficient control of iron hydr(oxide) nanoparticle formation onto the clay mineral surfaces constitutes the first key point of this work. Due to the key role played by organic matter in the formation of aggregates in soils and rivers, acting as gluing agent (Lai et al., 2018; Totsche et al., 2018), the third component had to be organic. In line with observations on particulate organic matter (Le Meur et al., 2017), a polysaccharidic polymer group was selected to mimic the organic constituent of our model aggregates. A neutral and relatively simple polymer was selected to promote the occurrence of hydrophobic interactions which are recurrently advanced to explain the reactivity of complex organo-mineral assemblies (Laird, 2001; Claret et al., 2002; Chenu et al., 2009; Hong et al., 2015; Gao et al., 2020). Dextran was selected as it was possible to vary the molecular weight of this organic molecule. We avoided the use of natural organic matter or humic acids as representative of the organic component in our micro-aggregates. This choice is motivated by a step-by-step strategy leading to a gradual and controlled increase in the complexity of the structure of the investigated assemblies. This option

is obviously far more complex to be achieved if using e.g. natural organic matter whose intrinsic reactivity properties are still controverted in literature (Town et al., 2012; Du et al., 2016). Even for relatively simple organic component as the one adopted in this work, the very order in the sequential addition of the various building units entering the composition of the prepared aggregates was itself central question. Based on literature review (Gao et al 2020) and observations of river SPM (Le Meur et al. 2017), we decided to prepare controlled organo-mineral assemblies with late addition of organic matter, using a neutral polymer. The developments below detail the preparation and the characterization of the resulting products, in particular the respective organization of the organic and mineral components of the generated assemblies.

2. Experimental

2.1. Pristine materials and chemicals

2.1.1. Clay minerals, illite.

The clay mineral used for all syntheses is the Illite from Puy-en-Velay, with prior purification and size-fractionation (Blachier et al., 2014). Purification was performed as follows: 40 g of clay were dispersed in one Litre of 1M sodium acetate solution adjusted to pH 5 upon addition of acetic acid 0.1 M. The suspension was heated to 80°C for 2 h, shaken during 12 h, and subsequently centrifuged for 20 min at 25 700 g (13000 rpm). The centrifuged paste was then re-dispersed in a sodium chloride solution (NaCl 1M) for 12 h to saturate the exchangeable sites with sodium and centrifuged twice for 20 min at 25 700 g. The resulting paste was then re-dispersed in ultrapure water for 12 h. Thus, the clay suspension was dialyzed to remove ions in excess (Spectra/Por® Membrane MWCO 50 kD). Dialysis was carried out until conductivity of the external solution was lower than 10 µS cm^{-1}. The dialyzed suspension was then centrifuged for 1 h at 25 700 g. The formed solid was subdivided according to two distinct fractions: the bottom, greyish, fraction was referred to as size fraction 2, the upper fraction, a greenish gel, was referred to as size fraction 3. In this work, only the gel fraction was considered, frozen and freeze-dried prior to synthesis experiments. X-Ray Diffraction (XRD) patterns obtained on pristine Illite evidenced the presence of impurities such as quartz and kaolinite clays (Data available on ORDAR repository https://doi.org/10.24396/ORDAR-28). Those minerals were almost totally removed with purification as shown by the XRD patterns obtained for the different size fractions. Size fraction 3 was noticeably homogeneous in terms of mineralogy and particle size. Cation Exchange Capacity (CEC) was determined using the cobalti-hexamine method (Ciesielski and Sterckeman, 1997). After exchange with cobalt hexamine and analysis with UV-Visible Spectrophotometer (UV2501-PC Shimadzu), the CEC was estimated to 20 meq per 100g of dry matter. This value corresponds to the estimated number of sites available for cationic exchange on clay surface. For all experiments, illite particles were dispersed for 4 hours at ambient temperature in 100 mL of ultra-pure water to obtain a final concentration of 200 mg L^{-1}. This clay concentration is consistent with the measured solid contents in river waters (Le Meur et al., 2016) and allowed us to perform multiple characterization measurements.

2.1.2.Chemical products

$Fe(NO_3)_3.9H_2O$ (quality: 0.9999) and KOH pellets from Aldrich were used for the preparation of clay-composites. The polymer is a polysaccharide, a Dextran from Leuconostoc ssp.**,** with molar mass 6000 g mol^{-1}, purchased from BioChemika (Supplementary Material SM-1). This is a relatively small polymer, constituted of about 33 sugar units, considering the molar mass of glucose (180.56 g mol^{-1}). Its Stoke radius is around 2 nm. For this molar mass range, Dextran molecules are supposed to behave as expandable coil. Dextran solutions were prepared at final concentrations 1.67 and 16.67 µmol L^{-1} (respectively 10 and 100 mg L^{-1}) with 5.10^{-4} M of $CaCl_2$

$2H_2O$ (Prolabo, quality: 0.99). In the particular case of illite-Dextran composites, the addition of calcium was mandatory to obtain the formation of aggregates. Without calcium addition, the illite-Dextran suspension remained stable even after 24h, and no size increase could be detected. The $CaCl_2$ concentration was selected on the basis of river water analysis (Le Meur et al., 2016) and also on the basis of suspension stability at 1h and 24h after Dextran addition (data not shown).

2.2. Preparation protocols

Three types of clay-composites were prepared, (i) illite-Fe (hydr)oxide referred to as $IFeH_R$, R being the Fe/illite ratio; (ii) illite-Dextran referred to as ID_x, x being the concentration of Dextran solution in mg L^{-1} and (iii) illite-Fe (hydr)oxide-Dextran referred to as $IFeH_RD_x$. A schematic presentation of the different preparation paths is provided in Supplementary material (SM-2).

2.2.1. Preparation of illite-Fe (hydr)oxide clay-composites $IFeH_R$ with R (the ratio iron/illite) = 0.2, 0.6 or 2. The main step of the preparation of illite-iron (hydr)oxide composites is the alkaline hydrolysis of iron salt (iron nitrate) in the presence of illite particles. The forced alkaline hydrolysis method was adapted from that of Schwertmann and Cornell (Schwertmann and Cornell, 1991). The resulting products are hereafter differentiated according to the initial iron/illite ratio, R. This ratio was calculated as a function of the CEC value of illite, and the amount of iron added to the clay suspension via:

$$R = (C_{\mathrm{I\,Fe}}\, V_{\mathrm{Fe\,ad}})/(C_{\mathrm{I}} V_{\mathrm{I}} CEC) \qquad (1)$$

where $C_{\mathrm{I\,Fe}}$ is the concentration of iron nitrate solution (10^{-4} M) expressed in meq of Fe per Litre and $V_{\mathrm{Fe\,ad}}$ the added volume of the iron nitrate solution ($V_{Fe,\,ad}$ = 2.7, 8 and 26.7 mL for R = 0.2, 0.6, 2, respectively). C_{I} (0.2 g L^{-1}) and V_{I} (100 mL) were the illite suspension concentration and volume, respectively. The CEC was measured and estimated to 20 meq per 100 g of illite. For the three R ratios adopted, the Fe/illite mass ratios were respectively 0.075, 0.22 and 0.75 mg Fe per g of illite. Experimental conditions were selected to promote the precipitation of iron (hydr)oxide onto the clay mineral surfaces rather than in solution. Iron nitrate concentration was fixed to 10^{-4} mol L^{-1}, KOH solution was set to 10^{-3} mol L^{-1} to slow down hydrolysis kinetics. Such pH and iron concentration conditions were expected to enhance the adsorption of either ferric cations or partially hydrolysed iron species on the cationic exchange sites of illite particles. The $Fe(NO_3)_3$ solution and KOH solution were simultaneously added to the illite suspension using a Metrohm TITRANDO 809 station. Such a procedure allowed controlled and reproducible synthesis conditions. Initial clay suspension displayed a pH close to 6. Iron solution (10^{-4}M, pH = 3.5) was added to the illite suspension at a rate of 0.25 mL min^{-1} until the desired Fe/illite ratio R was reached (R= 0.2, 0.6 or 2). Simultaneously, KOH was added at a rate of 0.1 mL min^{-1} until pH reaches 7.5 (± 0.2). Titration curves were performed several times (twice for $IFeH_{0.2}$ and $IFeH_2$, nine times for $IFeH_{0.6}$), and displayed a good reproducibility Supplementary Material SM-3. Subsequently, the resulting suspensions were washed by dialysis to remove salts in excess (Spectra/Por® Membrane MWCO 1 kD) until the suspension conductivity was close to that of ultrapure water (<10 µm S cm^{-1}). All rinsed precipitates were then freeze-dried and stored at 20°C prior to further analyses.

2.2.2. Preparation of illite-Dextran aggregates (ID_x). A supplementary series of binary samples was prepared to better evidence the influence of iron (hydr)oxides on the interactions between polymer and clay particles. For that purpose, binary aggregates composed of illite and Dextran polymer were prepared by adding simultaneously 50 mL of Dextran solution (x = 10 or 100 mg L^{-1}, i.e. 1.67 and 16.67 µmol L^{-1} respectively) and 50 mL of $CaCl_2.2H_2O$ solution to the illite suspension (200 mg L^{-1}). The mixture was stirred for 24 hours and repeatedly dialysed (Spectra/Por® Membrane MWCO 1 kD) until the suspension conductivity was close to that of ultrapure water (<10 µS cm^{-1}).

2.2.3. Preparation of illite-iron (hydr)oxide-Dextran aggregates (three component composites) referred to as $IFeH_RD_x$. The $IFeH_RD_x$ aggregates were prepared by addition of 50 mL of Dextran solution (x =10 or 100 mg L^{-1}) and 50 mL of 5.10^{-4} M $CaCl_2.2H_2O$ solution which contained a divalent ion promoting the aggregation of $IFeH_R$ particles in suspension. The mixture was stirred for 24 hours and repeatedly dialysed (Spectra/Por® Membrane MWCO 1 kD) until the suspension conductivity was close to that of ultrapure water (<10 µS cm^{-1}). Such a preparation procedure was adopted to obtain aggregates displaying the three constituents, i.e., illite, iron (hydr)oxides and organic polymer. The addition method was also established based on reported models of soil particle surfaces (see Gao et al. 2020 for instance).

2.3. Methods of characterization

2.3.1. Size distribution and electrophoretic mobility measurements. Electrophoretic mobilities (μ) and particle size distribution were measured for the final suspension of ID_x and $IFeH_RD_x$ and for the final dialyzed products in the case of illite and $IFeH_R$. A Zetasizer NanoZS (Malvern Instruments, UK) with a 633 nm laser source was used. For that purpose, one millilitre of final suspensions was placed in Malvern DTS1070 cells. The apparatus is well suited for measuring size of particles with diameter in the range of 1 nm to 6 µm and for monitoring electrophoretic mobility of particles with diameter from ca. 5 nm to 10 µm. The hydrodynamic diameter of particles was measured using dynamic light scattering (DLS). The particle diffusion coefficient was obtained from analysis of the autocorrelation of the scattered intensity measured at a 173° angle (back scattering) and converted into a hydrodynamic diameter using Stokes-Einstein equation. Electrophoretic mobility evaluation consisted in measuring velocity of charged particles in electrolyte suspension moving in a capillary cell under application of a DC electric field by Electrophoretic Light Scattering (ELS) technique. Zetasizer NanoZS device uses the M3-PALS procedure, combining Phase Analysis Light Scattering and a Mixed-Mode Measurement (M3). Using PALS, the particle velocity is obtained from the phase shift between light scattered by moving particles and a reference beam. The M3 technique, which combines two successive sequences of fast field reversal and slow field reversal, respectively, allows to overcome effects due to electro-osmosis that is generated by the coupling between hydrodynamics and surface charge of the capillary. Results were reported in the form of particle size distribution and electropherograms. In the developments that follow, electrophoretic mobility data were not converted into zeta-potential using e.g. standard Smoluchowski equation. The concept of zeta-potential makes physical sense for the only ideal scenario where particles are impermeable to ions and fluid flow. However, considering the permeability of soft particles such as the polysaccharide macromolecules used in this work, the concept of potential zeta cannot be applied (Duval et al., 2005, 2006; Duval, 2007; Martin et al., 2015).

2.3.2. Fourier Transform Infrared Spectroscopy (FTIR). FTIR spectra were collected on freeze-dried samples in Transmission (Tr) and Diffuse Reflectance (RD) modes using a Bruker Vector 22 FTIR spectrometer at a resolution of 4 cm^{-1}, in the 400-4000 cm^{-1} range. Samples were prepared from 1 mg of freeze-dried suspensions and were either deposited on a sheet of aluminium foil (for diffuse reflectance mode) or mixed with 199 mg KBr and pelletized (for transmission mode). Baseline-corrections were applied to collected spectra. An adjustment of the signals has been made for their better visualization and qualitative interpretation.

2.3.3. Transmission Electronic Microscopy (TEM) and Scanning Transmission Electron Microscopy (STEM). Samples for electron microscopy were prepared as follows: few dozens of µL of suspension was sampled and air-dried on a carbon-coated copper grid (200 mesh/100 µm) placed on a clamp. TEM and STEM investigations were performed at the Centre for Microscopies, Microprobes and Metallography (CC3M, Institut Jean Lamour, Nancy, France). As a first step, particles were investigated with a Philips CM200 TEM operated

at 200 kV. Beside transmission images, elemental composition of individual particles was determined using Energy Dispersive X-ray spectroscopy (EDXS) by means of a PGT (Princeton Gamma-Tech) spectrometer. The analyses were carried out in nanoprobe mode with a probe diameter of 50 nm.

High resolution transmission electron microscopy and scanning transmission electron microscopy (HRTEM and STEM) investigations were carried out using a JEM - ARM 200F Cold FEG TEM/STEM operating at 200 kV and equipped with a spherical aberration probe and image correctors (point resolution 0.12 nm in TEM mode and 0.078 nm in STEM mode). Images were recorded in Bright Field (BF) and High Angle Angular Dark Field modes (HAADF). EDXS spectra were recorded by means of a Centurio Jeol spectrometer (SDD) mounted on ARM 200F. The analyses were carried out in STEM mode with 1 nm probe diameter. The ratio between atomic percentages was estimated for semi-quantitative analysis. The Cliff Lorimer factors *k*, were determined using standards and were kept constant for each analysis.

2.3.4. X-ray absorption spectroscopy at Fe K-edge

To investigate the iron species resulting from alkaline hydrolysis of iron salt in presence of illite particles, X-ray absorption spectroscopy experiments at iron K-edge were conducted on SAMBA beamline (SOLEIL, France). XAS spectra were collected in transmission and fluorescence modes at low temperature using a liquid He cryostat 25K, with a Si(111) double crystal monochromator. Fe-illite composites were scanned at SAMBA in fly scan mode from 7000 to 8000 eV with 0.5 eV steps, at a velocity of 60 $eVsec^{-1}$, counting 0.08 sec per point. Samples were ground and pelletized before XAS measurements. XANES and EXAFS data were reduced using standard normalization procedures performed with the ATHENA and ARTEMIS programmes (Ravel and Newville, 2005). The spectra were background subtracted and normalized. A spline function was adopted to fit through the absorption envelope and then subtracted from each spectrum. To transform data from energy space E (eV) to wave vector space k ($Å^{-1}$), E_0 edge energy was chosen in the higher part of the edge step, at 7112 eV. The resulting $\chi(k)$ function was weighted by k^3 to avoid oscillations damping at high k values.

3. Results and discussion:

3.1. First series of binary clay-composites, illite-iron (hydr)oxide, $IFeH_R$.

3.1.1. Electrophoretic mobility and size of $IFeH_R$ aggregates.

Figure 1 reports size and electrophoretic mobility (μ) obtained for the iron-clay composites $IFeH_R$ as well as for the pristine illite clay particles. The analyses of pristine illite suspension showed particle sizes ranging between 60 and 500 nm with a maximum at 164 nm. For the three samples $IFeH_{0.2}$, $IFeH_{0.6}$ and $IFeH_2$, particle size distribution did not show drastic modification, thus evidencing that a large fraction of the clay platelets remained in suspension. For the three values of R considered in this work, clay particles aggregation was not evidenced as the size distribution patterns are similar to that obtained for illite particles. Indeed, only $IFeH_{0.2}$ and $IFeH_2$ samples presented a weak contribution of larger particles (size in the µm range). Concerning electrophoretic mobility measurements, the pristine illite particles displayed a rather broad distribution in μ values. The most frequent electrophoretic mobility value was -3.5×10^{-8} m^2 V^{-1} s^{-1}. This value had already been measured in low ionic strength solution (5 mM) (Beene et al., 1991; Sondi et al., 1996) and is mainly related to the permanent charge of the illite layers, and to a lesser extent, to the terminal groups located on the lateral edges (Thomas et al., 1999). For iron-illite samples, the electrophoretic mobility shifted to less negative values. This shift goes from -3.5 to -2.8×10^{-8} m^2 V^{-1} s^{-1} for $IFeH_{0.2}$, to -2.6×10^{-8} m^2 V^{-1} s^{-1} for $IFeH_{0.6}$ and to -2.4×10^{-8} m^2 V^{-1} s^{-1} for $IFeH_2$. This small but representative shift reflected the adsorption of hydrolysed Fe compounds on the cation exchange sites of illite. However, as the electrophoretic mobility of the iron-illite aggregates was of

the same order of magnitude as that of illite, the surface charge of the iron-clay composites remained dominated by the structural and permanent charge contribution of illite (Thomas et al., 1999).

3.1.2. Identification of iron species in IFeH$_R$ clay-composites.

X-ray Absorption spectroscopy at Fe K-edge, Transmission Electron Microscopy (TEM and HRTEM), and Scanning Transmission Electron Microscopy (STEM) were used to investigate iron species. Figure 2 presents EXAFS data obtained at Fe-K edge for the illite-FeH$_R$ samples. XANES spectra are provided as supplementary material (SM-4). The EXAFS curves are dominated by the signal of oxygen atoms, constituting the first coordination sphere, octahedrally coordinated to Fe. All EXAFS curves display similar features, with three oscillations centred at 4, 6.5 and 8.5 Å^{-1}. However, some differences can be observed between illite samples and FeH. The latter sample, resulting from the alkaline hydrolysis of a dilute solution of $Fe(NO_3)_3$, provides EXAFS signal attributed to ferrihydrite or precursors of ferrihydrite (Hofmann et al., 2013; Beauvois et al., 2020). The oscillation at 8.5 Å^{-1} is less intense for FeH than for illite and IFeH$_R$ samples. On the opposite, the shoulder at 7.5 Å^{-1} is more intense for FeH and reflects certainly the presence of iron atoms in the second coordination sphere. FeH sample provided relatively noisy signal due to the low amount of available sample for the measurement. IFeH$_R$ signals are all dominated by the illite contribution, without noticeable contributions of adsorbed Fe species.

Figure 3 displays selected micrographs obtained by HRTEM for pristine illite, and for the three illite-iron (hydr)oxide clay-composites, IFeH$_{0.2}$, IFeH$_{0.6}$ and IFeH$_2$ (supplementary images are presented in supplementary material SM-5). For pristine illite, individualized illite particles with well-defined edges could be observed. Most of the illite particles displayed their basal faces but some of them displayed the lateral faces, showing series of aluminosilicate layers (clearly visible with 200k magnification). The size distribution of illite particles derived from microscopy measurements (from 50 to 150 nm) agreed with the median hydrodynamic size reported in Figure 1. At 100k magnification (Figure 3, left images), some Fe nanoparticles with a stronger electron contrast could be detected for IFeH$_{0.6}$ and IFeH$_2$. Their presence of nanoparticles on the basal surfaces of illite for IFeH$_{0.6}$ and IFeH$_2$ samples is confirmed with higher magnification images (250 k). Again, Fe particles could not be detected on IFeH$_{0.2}$. Size distribution of Fe nanoparticles was rather heterogeneous as some of them were clearly visible at 100k magnification while most of those particles appeared only with higher magnification at 250 k. From those 250k images, the diameter of these Fe nanoparticles for IFeH$_{0.6}$ and IFeH$_2$ was estimated to be 5.6 ± 0.7 nm and 7.2 ± 1.7 nm, respectively. High magnification images also evidenced a drastic modification of illite particle aspect with increasing Fe/illite ratio. Indeed, the edges of clay minerals became less and less defined and the particles displayed a lumpy appearance due to iron precipitation. The presence of the nano-FeH on illite surfaces indicated that the growth of iron (hydr)oxide had occurred on the illite surfaces and that the nucleation of iron (hydr)oxide was constrained by the presence of illite particles. With increasing Fe/illite ratio, iron precipitation could occur not only on basal surfaces but also on lateral sites, which would explain the loss of definition of illite edges.

FeH$_R$ samples were also analysed in STEM mode, providing Bright Field (BF) and High-Angle Annular Dark-Field (HAADF) images (Figure 4). In HAADF mode, the increase in brightness indicated an increase in atomic number (Z contrast, increase of electronic density) due to the presence of iron (hydr)oxide particles. Both BF and HAADF modes revealed the presence of nanometric entities at the surface of the clay platelets for all IFeH$_R$ samples including IFeH$_{0.2}$. The detected Fe entities displayed a mean size of 2 nm (± 0.5 nm) for the IFeH$_{0.2}$ and IFeH$_{0.6}$ samples. In the case of IFeH$_2$, two sets of particles could be evidenced, one with a similar mean size of 2 nm, and another set of particles with a mean size of 8 nm (±1 nm).

The Fe/Si atomic ratio was estimated from EDXS data obtained on CM200 microscope. For $IFeH_{0.2}$, $IFeH_{0.6}$ and $IFeH_2$, this ratio was 0.102 ±0.01 ,0.097±0.01 and 0.107±0.01, respectively, calculated from 10, 14 and 3 analyses respectively. Those Fe/Si atomic ratios do not show a clear trend with the increase of initial Fe/illite ratio and finally are close to that obtained for the pristine illite particles (0.095±0.01, 6 analyses). Even though Fe nanoparticles could be observed from TEM or STEM images, the atomic percentage of iron did not increase significantly. The size range of these Fe nanoparticles prevented their detection by classical TEM and associated EDXS. The nanoprobe used for EDXS was set between 50 and 100 nm, about ten times larger than the nanoparticles of iron (hydr)oxide. This explains why the illite signal predominates the EDXS spectra. Supplementary EDXS data obtained on the HRTEM microscope using a smaller nanoprobe (few nanometres), demonstrated more clearly the increase in Fe/Si ratio (≥0.10) for $IFeH_{0.2}$ and $IFeH_{0.6}$ samples (see table in SM-5), thereby confirming the presence of nanoparticles of iron-hydr(oxide). None of the EDXS spectra obtained on both microscopes evidenced the presence of isolated iron hydr(oxide) for the three samples $IFeH_{0.2}$, $IFeH_{0.6}$ and $IFeH_2$. Both images and EDXS data obtained on ARM microscope demonstrated the formation of nanoFeH onto the surface of illite, and the size limitation demonstrated that the formation of iron (hydr)oxide was constrained by the interaction with the clay surface. The presence of surface hydroxyl groups, acted as ligands in solution (Lartiges et al., 2019 and references therein). The titration of iron solution in the presence of an organic and/or mineral component had already shown that hydrolysis and nucleation of iron in solution were limited by these components, which explained the formation of iron (hydr)oxides of nanometer size (Mikutta and Kretzschmar, 2008; Guénet et al., 2017; Lartiges et al., 2019; Beauvois et al., 2020). The interaction of iron species with illite surface (via electrostatic interactions with the exchangeable sites, and with lateral hydroxyl groups) had reduced the OH substitution and had prevented the formation of larger Fe (hydr)oxide particles.

3.1.2. Influence of illite surface on the hydrolysis of iron.

Previous publications reported the synthesis and characterization of hybrid particles based on montmorillonite and iron oxides (Ferreiro et al., 1995; Green-Pedersen and Pind, 2000; Ji et al., 2004; Borgnino et al., 2009). Borgnino and Green-Pedersen produced Fe-clay using a similar method, by alkaline hydrolysis of ferric salt in the presence of clay particles. Although they display similar features, illite and montmorillonite presents a different lateral/basal surface ratio, and different cation exchange capacities (CEC). Illite particles are thicker, and their basal plane is less extended, the CEC of illite is about five times lower than that of montmorillonite. Such differences strongly enhanced the interactions of iron with OH groups from the lateral edges of illite particles. This point was demonstrated for high iron/illite ratios, as a modification of edge appearance was evidenced (HRTEM, Figure 3).-Three mechanisms can be envisaged for iron hydrolysis in the presence of clay particles: either (1) alkaline hydrolysis of iron, nucleation in solution and formation of nanoFeH in bulk solution followed by adsorption on the Illite particles, or (2) adsorption of partially hydrolysed Fe(III) cations (with excess charge ranging from +1 to +3) and/or Fe-oligomers on the illite particles, followed by nucleation and formation of nanoFeH, or (3) concomitant occurrence of these two latter reactions. The exact nature of the adsorbed Fe species during the titration needs to be debated. Supplementary material (SM-3) shows the three titration curves obtained respectively for $IFeH_{0.2}$, $IFeH_{0.6}$ and $IFeH_2$. The titration curves showing pH evolution as a function of the addition of KOH are rather similar. Illite particles appear to be the main OH consumers in the second part of the titration curve. Such an observation tends to support that the Fe species were already hydrolysed in solution prior to adsorption onto clay illite. However, the similarity of the titration curves, irrespectively of the iron concentration, could also be explained by the low amount of iron added in solution, insufficient to impact on the form of the titration curve.

To conclude, the synthesis conditions of $IFeH_{0.2}$ have enhanced the formation of iron oligomers in solution before adsorption of iron species onto the clay surface, and subsequent nucleation and formation of nanoparticles of iron (hydr)oxide, nanoFeH, have further occurred onto the clay basal surfaces.

For the higher Fe/illite ratios tested, R=0.6 or 2, there is a questioning about the formation process of iron (hydr)oxide. The presence of lateral nanoFeH could result from either the hydrolysis of pre-adsorbed iron or the adsorption of nanoFeH. The formation of covalent bonds between Fe atoms and the octahedral sheet of illite have prevented the hydrolysis, i.e. the replacement of H_2O molecules by OH, and might have prevented the olation and oxolation reactions that lead to the formation of nanoFeH. Then, we assumed that the lateral nanoFeH were formed in solution and were finally adsorbed on the illite edges.

All in all, regardless their precise formation mechanism, the status of iron species adsorbed onto the illite particles was dominated by nanoFeH forms as evidenced by STEM observations, and this conclusion held for all $IFeH_R$ samples. One supplementary concluding remark about the illite-FeH composites is the moderate modification of their size and electrophoretic mobility (compared to illite). As mentioned above, the Fe/illite ratio used for our experiments was not sufficient to shield the repulsive interactions between negatively charged illite platelets (Beene et al., 1991; Lin et al., 2017). Then, iron hydr(oxide) particles present in the $IFeH_R$ are closely associated with illite particles, forming size-reduced particles covering the illite surface.

3.2. Illite-Dextran aggregates, ID_x.

To evidence the influence of iron coatings on the interactions between clay particles and the organic polymer Dextran, a second set of clay-composites was prepared without iron (hydr)oxide, using only illite and Dextran. Dextran concentrations from 1.67 and to 16.67 µmol L^{-1} were selected to produce illite-Dextran aggregates. The endmembers of this sample series are referred to as ID_{10} and ID_{100}, respectively. Dextran was always added simultaneously with $CaCl_2$ as preliminary tests demonstrated that Dextran alone was not able to flocculate the illite particles (those tests were based on the monitoring of the turbidity of the suspension, data not shown). Figure 6 compares size and μ distributions obtained after the addition of both Dextran and $CaCl_2$. The same measurements were performed after the addition of $CaCl_2$ alone. $CaCl_2$ addition caused a clear and well-marked increase in particle size distribution (supplementary material SM-6). The size distribution was shifted towards higher values, with a broad band centred in 1718 µm. Moreover, there was a weak contribution of smaller particles, with a broad band centred at 250 nm. The electrophoretic mobility of illite particles after $CaCl_2$ addition was further shifted towards lesser negative values, with a central value at -1×10^{-8} m^2 V^{-1} s^{-1}. The presence of Ca^{2+} in solution screened the repulsive interactions between negatively charged illite particles. Such an electrostatic screening was already reported in numerous publications (Jellander et al., 1988; Jiang et al., 2012; Kloster and Avena, 2015 and references therein). The illite-Dextran aggregates (Figure 5) displayed similar size distribution and electrokinetic properties compared to those obtained after addition of $CaCl_2$. Any increase in Dextran concentration did not bring any modification to the resulting size and μ distributions. Modifications of size and electrophoretic mobility of illite upon addition of Dextran and Ca^{2+} were mainly explained by the shielding of clay charge, due to the saturation of illite exchange sites by divalent cations. Furthermore, the addition of divalent cations was leading to a shift of μ to a value close to that of Dextran, thus minimizing the range of eventual modifications of electrokinetic properties because of sole Dextran adsorption to illite particles. Therefore, at this stage, we could not conclude on the occurrence and type of interactions between Dextran and illite particles.

To monitor Dextran content, FTIR spectra were collected in two measurement modes, transmission (Tr), and diffuse reflectance (DR) (Figure 6). The former provides quantitative chemical information on the whole illite-Dextran aggregate (ID_x) and the relative contents of mineral and organic components. The latter is particularly

sensitive to surface composition (about few nanometres are estimated to be probed with this technique considering the water content of samples) (Milosevic and Berets, 2002; Madejová, 2003; Armaroli et al., 2004).

Figure 6 presents the high wavenumber range of the FTIR spectra. The low wavenumber range of those spectra are presented as supplementary material (SM-7). In transmission mode (Figure 6top graph), the vibration bands of illite (ν_{OH} 3698 and 3620 cm-1) were visible for each of the samples tested and so were the bands corresponding to Dextran (ν_{CH2} 2954 and 2930 ν_{CH} 2890 and 2855 cm^{-1})). The intensity of the bands assigned to Dextran is low for ID_{10} sample and Dextran signature in the 1500-1000 cm^{-1} wavenumber range is hardly detected (SM-7). With increasing Dextran concentration (ID_{100}), Dextran vibration bands increase in intensity, in line with expectation. These FTIR spectra were acquired for three distinct series of IDx samples with *x* initially fixed to 5, 10, 20, 50 and 100, providing reproducible results. To estimate the illite/Dextran ratio, the ratios of intensity bands respectively centred in 3698 and 2930 cm^{-1} were calculated. This ratio decreases from 3.05 to 0.71 for ID_{10} and ID_{100}. Beside intensity, the stretching vibration bands of alkyl groups (ν_{CH2} and ν_{CH}, 3000-2800 cm^{-1}) were modified for ID_{10} sample. Those stretching vibrations are clearly separated for ID_{10} whereas pure Dextran displays a broad band centred in 2930 cm^{-1} and a shoulder at 2890 cm^{-1} (Figure 6 and supplementary material SM-1). Such modifications of Dextran signal were assigned to interactions with illite surface (through Ca^{2+} bridges). Previous experiments on Dextran-montmorillonite aggregates had also revealed a close association of polymer with clay mineral surfaces (Labille et al., 2005) and experiments on humic adsorption with different loads of Ca had also evidenced the crucial role of Ca (Kloster and Avena, 2015).
For ID_{100} the splitting of the ν_{CH} and ν_{CH2} bands is no longer observed, and the Dextran signal is basically similar to that of pure Dextran. This observation is further confirmed upon inspection of the spectra in the low wavenumber range. At such high Dextran concentrations, majority of the polymer chains did not interact with the illite minerals and bulk Dextran phase showed up in the aggregate.
In diffuse reflectance mode (Figure 6, bottom graph), the vibration bands of illite are present and so are the bands corresponding to Dextran. We observed for ID_{10} the same shift of the ν_{CH} band as in transmission mode, showing a modification of vibration bands of the polymer due to interactions between Dextran and the surface of illite particles. For ID_{100}, the intensity of the Dextran peaks increased with no deviation of the bands in the stretching vibration range (ν_{CH2} 2930 cm^{-1} and ν_{CH} 2890 cm^{-1}). The absence of peak modification in the stretching vibration range (ν_{CH2} 2930 cm^{-1} and ν_{CH} 2890 cm^{-1}) in diffuse reflectance mode was reported in the literature for other organo-clay mixtures (Webb et al., 1986; Mpofu et al., 2004). ID_{100} FTIR spectra evidenced the presence of Dextran on the surface of aggregates with low or no interaction with illite.

While Transmission FTIR spectra showed that Dextran was present within the aggregates and was in interaction with the clay platelets, Diffuse Reflectance spectra evidenced that Dextran and illite were both present at the surface of aggregates. Although the Dextran content is low for ID_{10} (roughly estimated between 5 and 10% from a linear combination of transmission spectra of Dextran and illite), Diffuse Reflectance spectrum confirmed the presence of the polymer on the external surface of the aggregates. Since ID_{10} FTIR-DR spectrum evidenced the contribution of illite, we concluded that few illite particles remained as pristine illite, i.e. without Dextran. The average diameter of Dextran, which is assumed to be cylindrical under the conditions of aggregate preparation, is about 2-3 nm. Illite particles display a length of about 87±25 nm, a width of about 58±13 nm and a thickness of 18±7 nm (from TEM and HRTEM data). Dextran entities are smaller than illite particles and cover only partially the surfaces of the clay platelets. For ID_{100}, the relatively high amount of adsorbed Dextran was evidenced by transmission and explained the absence of shift of Dextran vibration bands in diffuse reflectance mode. Dextran contribution to FTIR spectrum was roughly estimated to 50 % through the same method based on linear

combination of referenced spectra. With these results at hand, the now-demonstrated presence of Dextran at the surface of illite particles is unseen in the size and electrokinetic measurements (Figure 5).

To explain the apparent low contribution of Dextran in the ID_{10} FTIR signal, the micrometric size of aggregates should be considered. Diffuse Reflectance spectra demonstrated the position of Dextran at the external surface of aggregates. Thus, it can be concluded that those illite-Dextran aggregates display a dense core mainly constituted of illite platelets, aggregated by Ca^{2+} ions. It can also be concluded that the Dextran molecules are loosely attached to the surface, through Ca^{2+} bridges as it was suggested for montmorillonites (Labille, 2003; Labille et al., 2005). In the case of swelling clays such as montmorillonite, multivalent cations reduce the energy barrier separating montmorillonite particles. For illite particles, displaying a charge density twice higher than that of montmorillonite layers, similar reactions were enhanced by Ca^{2+} (Jiang et al., 2012; Kloster and Avena, 2015; Lin et al., 2017). Ca^{2+} ions occupy exchange sites on the surface of illite minerals and finally allow the adsorption of Dextran simultaneously on several particles via weak interactions between the OH groups of Dextran and the water molecules of the hydration sphere of the Ca^{2+} cations.

3.3. Ternary aggregates, illite-Iron (hydr)oxide-Dextran $IFeH_RD_x$:

Two series of $IFeH_RD_x$ aggregates were respectively prepared from $IFeH_{0.6}$ and $IFeH_2$ clay-composites. Figure 7 reports the results of size and electrophoretic mobility distributions for $IFeH_{0.6}D_x$ samples and compares them with data collected for the binary sample $IFeH_{0.6}$. Here, the addition of $CaCl_2$ and Dextran caused an increase in particle size, similarly to what was observed for ID_x aggregates (Figure 5).

The particle size of $IFeH_{0.6}D_{10}$ ranges between 100 nm and 3 µm with a maximum at 955 nm, showing a clear aggregation of illite-FeH particles. Increasing the amount of added Dextran leads to two populations of aggregates, relatively large aggregates with size in the 0.4-3 µm range and smaller ones in the 100-400 nm range. The electrophoretic properties of $IFeH_{0.6}$ are modified upon addition of $CaCl_2$ and Dextran. There is indeed a clear shift in mobility towards lesser negative values. The mobility distribution is centred around -1.6 x 10^{-8} m^2 V^{-1} s^{-1} for $IFeH_{0.6}D_{10}$ instead of -2.6 x 10^{-8} m^2 V^{-1} s^{-1} for $IFeH_{0.6}$. Addition of larger amount of Dextran to $IFeH_{0.6}$ results in a similar shift, except that the distribution of μ values for the resulting $IFeH_{0.6}D_{100}$ product is now centred at -1.8 x 10^{-8} m^2 V^{-1} s^{-1}, and it is broader than that for $IFeH_{0.6}D_{10}$.

Overall, the addition of $CaCl_2$ and Dextran to $IFeH_{0.6}$ did not provoke the formation of large aggregates as we could observe for the systems illite+Ca^{2+} or IDx samples, and the shift in mobility was less pronounced than that observed when $CaCl_2$ and Dextran were added to Illite alone (Figure 5). Last, the increase in Dextran concentration leads to smaller particles as the curve displays a clear contribution centred at 210 nm. It is therefore apparent that the presence of iron nanoparticles on the illite surfaces modified their surface reactivity.

The addition of $CaCl_2$ and Dextran to $IFeH_{0.6}$ and $IFeH_2$ samples was followed by FTIR in Transmission and Diffuse Reflectance modes (Figure 8). To unravel the influence of nanoFeH on Dextran adsorption and on the respective organization of Dextran and clay platelets within the formed assemblies, two sets of aggregates prepared from $IFeH_{0.6}$ and $IFeH_2$ were considered.

FTIR spectra collected for ID_{10}, $IFeH_{0.6}D_{10}$ and $IFeH_{02}D_{10}$ samples (top graphs), all prepared with a Dextran concentration set at 10 mg L^{-1}, are presented on Figure 8 in both transmission and diffuse reflectance modes (low range of FTIR spectra are presented in figure SM-7B) Those spectra revealed the vibration bands of illite and Dextran in the stretching domain. With increasing iron content ($IFeH_2D_{10}$, Figure 8 curve c), the vibration bands of illite (ν_{OH} 3620 cm^{-1}) became less visible while vibration bands of Dextran are more intense. Moreover, the sample $IFeH_2D_{10}$ exhibited a higher amount of water than in $IFeH_{0.6}D_{10}$, as judged by the broad and intense stretching band of OH centred at 3400 cm^{-1}. This higher amount of water in the sample related to the higher

content of Dextran. For the three samples analysed, the stretching vibration bands of alkyl groups (3000-2800 cm^{-1} range) appeared in the form of separated bands, centred at 2954, 2930 and 2890 cm^{-1}. However, the splitting of these signatures was as pronounced as that identified for $IFeH_{0.6}D_{10}$. To quantify the influence of nanoFeH on Dextran adsorption, intensities ratios were calculated. The intensity ratio I_{3698}/I_{2930} compared the contribution of illite and Dextran to the signal and this ratio decreased from ID_{10} to $IFeH_{0.6}D_{10}$ and $IFeH_2D_{10}$, with the respective values 3.05, 1.49 and 0.77. Although these intensity ratios cannot be used for an exact quantification of Dextran content or of the illite/Dextran ratio, the calculation of such intensity ratios was useful to compare the different samples.

The Diffuse Reflectance spectra (bottom graph in Figure 8) revealed the same trend between the three samples, demonstrating that the presence of iron particles had modified Dextran adsorption. Indeed, $IFeH_{0.6}D_{10}$ spectrum showed that the amount of Dextran in the external zone of the aggregates is higher than for ID_{10}. However, the contribution of illite bands to the DR-FTIR signal suggested, similarly to ID_{10}, that the surface of illite particles was partially visible and not covered by Dextran. Also, the splitting of the stretching bands of Dextran was even more marked in DR than in Transmission mode, thus suggesting a stronger interaction between mineral entities and Dextran OH groups.

For ternary aggregates built from $IFeH_2$ (Figure 8 spectrum c), the presence of Dextran in the external region of aggregates was clearly unravelled from the Transmission and Diffuse Reflectance FTIR spectra. The stretching bands of Dextran (2800-3000 cm^{-1}) were no longer separated for $IFeH_2D_{10}$, therefore suggesting that a major proportion of Dextran chains did not experience interactions with the mineral surfaces. The comparison between $IFeH_{0.6}D_{10}$ and $IFeH_2D_{10}$ spectra showed that the increase in amount of iron hydr(oxide) nanoparticles enhanced the insertion of Dextran within the aggregates. In addition, the presence of iron nanoparticles also impacted on the spatial distributions of clays and polysaccharide units in the aggregates. The differences between $IFeH_{0.6}D_{10}$ and $IFeH_2D_{10}$ spectra were more pronounced in diffuse reflectance mode than in transmission mode. As far as the aggregates were concerned, the adsorption of Dextran was not only enhanced by nanoFeH, but its location was also shifted towards the outer surface of the aggregates.

Similar spectra with higher concentration in Dextran (100 mg L-1) can be found in supplementary material (figure SM-8). For the samples prepared with a higher concentration of Dextran (100 mg/L)the vibration bands of illite OH groups were hardly detected. Moreover, the intensity ratio I_{3698}/I_{2930} reflecting the respective contributions of illite and Dextran signals basically decreased if compared to that for the previous series of aggregates prepared with 10 mg/L Dextran: this ratio was further slightly decreasing from ID_{100} to $IFeH_{0.6}D_{100}$ and $IFeH_2D_{100}$, with the respective values 0.71, 0.57 and 0.5. In addition, in transmission mode the vibration bands of Dextran in the stretching region were split for $IFeH_{0.6}D_{100}$ and $IFeH_2D_{100}$, which supported that OH groups carried by the polymer were constrained through interactions with illite surface and/or nanoFeH entities. This splitting was not observed for ID_{100} and disappeared in Diffuse Reflectance mode for all $IFeH_RD_{100}$ samples. Moreover, the Diffuse Reflectance spectra evidenced the fading away of illite signal, replaced by Dextran and associated water. At sufficiently high polymer concentrations (100 mg L^{-1}), iron particles appeared to have no influence on the adsorption and on the organization of Dextran within the aggregates, suggesting that the nano-Fe adsorption sites for Dextran were saturated.

The above Diffuse Reflectance observations evidenced that the contribution of illite entities to FTIR signal was significantly screened due to enhanced adsorbed amount of Dextran. These observations also indicated that the higher the Dextran content was, the lower became the fraction of Dextran chains interacting with the mineral surfaces.

3.4. Influence of nanoFeH on illite-Dextran interactions

The addition of Ca^{2+} and Dextran to illite-FeH aggregates did not produce similar results than the addition of these components to bare illite particles. First, considering the size distributions and FTIR data (Figures 5 to 8) the comparison between ID_{10} and $IFeH_{0.6}D_{10}$ shows a reduction of aggregate size as well as an increase of the Dextran/illite ratio for the latter system. Since Transmission FTIR collected the signal from the whole aggregate, this apparent increase of Dextran content can be explained by the reduction of the aggregate size, i.e. the contribution of the illite core is diminished and the signal from the peripheral part of the aggregates is enhanced. The modifications in μ showed that the presence of nanoFeH reduced the interactions of Ca^{2+} with illite particles (Figures 5 and 7). Indeed, without nanoFeH, μ was shifted by ca. 2.5 x 10^{-8} m^2 V^{-1} s^{-1}, while it was only shifted by 1 x 10^{-8} m^2 V^{-1} s^{-1} for samples exhibiting nanoFeH.

The presence of nanoFeH on the basal surfaces of illites diminished the effect of Ca^{2+}, reduced the screening effect and limited the flocculation reaction. Diffuse reflectance spectra evidenced an external positioning of Dextran (Figure 9), but the polymer did not modify the electrophoretic mobility. As it was previously suggested by measurements on ID_x aggregates, calcium adsorption on the clay minerals mainly governs the end electrokinetic properties of the aggregates.

The splitting of the size distribution pattern observed for $IFeH_{0.6}D_{100}$ (Figure 6) can be explained by the amount of Dextran integrated within the aggregates, itself depending on the amount of nanoFeH on the clay surface. We can apply the same reasoning as for $IFeH_{0.6}D_{10}$. Indeed, the formation of sub-micrometric aggregates (centred in 250 nm) with higher Dextran content strongly suggests that Dextran adsorption was promoted by nanoFeH. The smaller size of aggregates can be explained by the heterogeneous distribution of nanoFeH on illite surface as shown by TEM images. NanoFeH particles occupied cation exchange sites and reduced the electrostatic interaction of Ca^{2+} cations with illite particles.

The apparent higher amount of adsorbed Dextran is related to the presence of nanoFeH on the surface of illite platelets, which leads to the following questions: what is the exact mechanism of aggregate formation and what is the exact role played by nanoFeH? The affinity of iron oxides for organic matter was reported in numerous studies (Reinhardt and Wilkinson, 2004; Cloy et al., 2014; Vindedahl et al., 2016; Sowers et al., 2018b), so that it is likely that the presence of nanoFeH enhanced Dextran adsorption. For Fe-montmorillonite hetero-aggregates (Ji et al., 2004), it was suggested that the presence of FeH reduced the charge and electric field of clay particles. Such a reduction of clay mineral charge reduced the repulsive forces acting between illite and Dextran molecules, thereby promoted Dextran adsorption. Such an explanation might not be accepted for the current case of illite-nanoFeH aggregates for two reasons. First, the charge density of the illite particles is twice higher than that of montmorillonite, and second because the ratio iron/clay used for our study was far lower than that of Ji et al.

Supported by these results obtained on three different types of aggregates, different assembly schemes can be proposed (Figure 9). Binary aggregates ID_{10} appear as large aggregates or large Ca-illite flocs with low electrophoretic mobility values (in magnitude) due to the significant screening exerted by Ca^{2+} ions. They display a rather low amount of Dextran as revealed by FTIR. The polymer interacts with the mineral surfaces though Ca^{2+} bridges and shows preferential localization on the external surface of the Ca-illite flocs.

Ternary aggregates $IFeH_{0.6}D_{10}$ and $IFeH_{0.6}D_{100}$ display different properties. The presence of iron oxy-hydroxide nanoparticles on the surface of the illite particles not only diminished the adsorption of Ca^{2+} and subsequently limited the floc growth but also enhanced the adsorption of Dextran. $IFeH_{0.6}D_{10}$ is constituted of aggregates of 900 nm size, with a charge that is screened by Ca^{2+} adsorption. The Dextran content is slightly higher than for ID_{10} and as for ID_{10} sample, the polymer shows interaction with mineral entities (nanoFeH or

illite). Increasing Dextran concentration ($IFeH_{0.6}D_{100}$) lead to aggregates of similar size.Supplementary Dextran molecules in the periphery of the aggregates did not develop interactions with mineral entities (FTIR data on Figure 8 and SM-8). Furthermore, $IFeH_{0.6}D_{100}$ sample displayed additional smaller aggregates with higher Dextran content. The presence of these smaller aggregates can be explained by the heterogeneous distribution of nanoFeH. Illite platelets with a denser Fe coating may adsorb higher amounts of Dextran, limiting the interactions with other clay platelets.

4. Conclusions:

Our main objective was to prepare and characterize ternary aggregates built from the addition of an organic polymer, a neutral polysaccharide, to a suspension of illite particles coated by iron (hydr)oxide nanoparticles. To understand the spatial assembly of the three components and highlight the influence of iron coating, we analysed three distinct types of aggregates based on the modification of clay particles through the addition of iron coating and/or Dextran to illite suspension. Such a step-by-step investigation of binary and ternary aggregates was particularly relevant to explore the respective organizations of the different components involved in the formed organo-mineral composites. In addition, the combination of electrokinetic and spectroscopic data has been proven fruitful to elaborate assumptions regarding the way organic and mineral components interact. Two main results can be highlighted:

- the formation of nanoFeH onto illite particles could be evidenced, and such illite-FeH aggregates were synthesized under pH conditions close to neutrality with use of relatively low concentrations of both iron and clay minerals. The preparation conditions were selected to be more realistic -from an environmental perspective- than those adopted in previously published reports.
- the interactions between clay minerals and a neutral polysaccharide were shown to be favoured by the presence of nanoFeH.

Our study further sheds light on the processes driving hydrolysis of iron in the presence of clay minerals. We indeed evidenced the role of illite particles in the nucleation mechanism of ferrihydrite. This work on iron-clay composites should be completed by a systematic investigation of the influence of layer charge (density and localisation), or the influence of the clay shape and size. Moreover, to mimic the complex structure of natural aggregates as found in river SPM, the use of more complex organic representatives like humic or fulvic acids should be carried out. Also, considering the diversity of organic molecules in environmental media, the use of several organic materials for the preparation of clay-based aggregates should be the next step. Our results are based on the recourse to different characterization techniques but call for supplementary investigations. In the future, larger amounts of clay composites will be prepared to investigate the surface properties using gas probes to determine surface area and pore volume distribution. Finally, these preliminary works on ternary aggregates pave the way for more complex systems, including further investigations of the aggregates formation and reactivity.

Acknowledgements:

This study is part of a Ph.D. work financially supported by the French Administrative Region Grand-Est and by the French Ministry of Higher Education and Research. This work was performed with the financial support of the Zone Atelier Moselle (ZAM), belonging to the French Zones Ateliers Network (RZA) driven by CNRS INEE institute. We are very grateful to Jaafar GHANBAJA and Sylvie MIGOT from Institut Jean Lamour in Nancy (France) for their strong support for Transmission Electron Microscopy. We thank Delphine VANTELON (SOLEIL) and Martine MALLET (LCPME) for their constructive discussions about this Ph.D. work. We also acknowledge SOLEIL for provision of synchrotron radiation facilities, and we would like to thank

Gauthier LANDROT for assistance in using beamline SAMBA. We are grateful to Manuel PELLETIER (LIEC) for his constructive comments on FTIR interpretation and to Christophe GAUTHIER (LIEC) for his help in running XAS experiments at SAMBA beamline. We also thank the reviewers for their constructive comments on this manuscript.

References:

Adhikari, D., Sowers, T., Stuckey, J.W., Wang, X., Sparks, D.L., Yang, Y., 2019. Formation and redox reactivity of ferrihydrite-organic carbon-calcium co-precipitates. Geochim. Cosmochim. Acta 244, 86–98. https://doi.org/10.1016/j.gca.2018.09.026

Armaroli, T., Bécue, T., Gautier, S., 2004. Diffuse reflection infrared spectroscopy (DRIFTS): Application to the in situ analysis of catalysts. Oil Gas Sci. Technol. 59, 215–237. https://doi.org/10.2516/ogst:2004016

Beauvois, A., Vantelon, D., Jestin, J., Rivard, C., Bouhnik-Le Coz, M., Dupont, A., Briois, V., Bizien, T., Sorrentino, A., Wu, B., Appavou, M.-S., Lotfi-Kalahroodi, E., Pierson-Wickmann, A.-C., Davranche, M., 2020. How does calcium drive the structural organization of iron–organic matter aggregates? A multiscale investigation. Environ. Sci. Nano 7, 2833–2849. https://doi.org/10.1039/D0EN00412J

Beene, G.M., Bryant, R., Williams, D.J.A., 1991. Electrochemical properties of illites. J. Colloid Interface Sci. 147, 358–369. https://doi.org/10.1016/0021-9797(91)90168-8

Blachier, C., Jacquet, A., Mosquet, M., Michot, L., Baravian, C., 2014. Impact of clay mineral particle morphology on the rheological properties of dispersions: A combined X-ray scattering, transmission electronic microscopy and flow rheology study. Appl. Clay Sci. 87, 87–96. https://doi.org/10.1016/j.clay.2013.11.004

Borgnino, L., Avena, M., De Pauli, C., 2009. Synthesis and characterization of Fe(III)-montmorillonites for phosphate adsorption. Physicochem. Eng. Asp. 341, 46–52. https://doi.org/10.1016/j.colsurfa.2009.03.037

Buffle, J., Wilkinson, K.J., Stoll, S., Zhang, J., 1998. A Generalized Description of Aquatic Colloidal Interactions : The Three-colloidal Component Approach. Environ. Sci. Technol. 32, 2887–2899. https://doi.org/10.1021/es980217h

Chenu, C., Virto, I., Plante, A., Elsass, F., 2009. Clay-size organo-mineral complexes in temperate soils: Relative contributions of sorptive and physical protection, in: Laird, D.A., Cervini-Silva, J. (Eds.), CMS Workshop Lectures, Carbon Stabilization by Clays in the Environment: Process and Characterization Methods. Clay Mineral Society, Chantilly, VA, pp. 120–135. https://doi.org/https://doi.org/10.1346/CMS-WLS-16

Churakov, S. V., Dähn, R., 2012. Zinc adsorption on clays inferred from atomistic simulations and EXAFS spectroscopy. Environ. Sci. Technol. 46, 5713–5719. https://doi.org/10.1021/es204423k

Ciesielski, H., Sterckeman, T., 1997. Determination of cation exchange capacity and exchangeable cations in soils by means of cobalt hexamine trichloride. Effects of experimental conditions. Agronomie 17, 1–7. https://doi.org/10.1051/agro:19970101

Cismasu, A.C., Michel, F.M., Stebbins, J.F., Levard, C., Brown, G.E., 2012. Properties of impurity-bearing ferrihydrite I. Effects of Al content and precipitation rate on the structure of 2-line ferrihydrite. Geochim. Cosmochim. Acta 92, 275–291. https://doi.org/10.1016/j.gca.2012.06.010

Cismasu, A.C., Michel, F.M., Tcaciuc, A.P., Brown, G.E., 2014. Properties of impurity-bearing ferrihydrite III. Effects of Si on the structure of 2-line ferrihydrite. Geochim. Cosmochim. Acta 133, 168–185. https://doi.org/10.1016/j.gca.2014.02.018

Claret, F., Bauer, A., Schäfer, T., Griffault, L., Lanson, B., 2002. Experimental investigation of the interaction of clays with high-pH solutions: A case study from the Callovo-Oxfordian formation, Meuse-Haute Marne underground laboratory (France). Clays Clay Miner. 50, 633–646. https://doi.org/10.1346/000986002320679369

Cloy, J.M., Wilson, C.A., Graham, M.C., 2014. Stabilization of organic carbon via chemical interactions with Fe and Al oxides in gley soils. Soil Sci. 179, 547–560. https://doi.org/10.1097/SS.0000000000000096

Colombo, C., Torrent, J., 1991. Relationships between aggregation and iron oxides in Terra Rossa soils from southern Italy. Catena 18, 51–59. https://doi.org/10.1016/0341-8162(91)90006-J

Du, H., Chen, W., Cai, P., Rong, X., Dai, K., Peacock, C.L., Huang, Q., 2016. Cd(II) Sorption on Montmorillonite-Humic acid-Bacteria Composites. Sci. Rep. 6. https://doi.org/10.1038/srep19499

Du, H., Peacock, C.L., Chen, W., Huang, Q., 2018. Binding of Cd by ferrihydrite organo-mineral composites: Implications for Cd mobility and fate in natural and contaminated environments. Chemosphere 207, 404–412. https://doi.org/10.1016/j.chemosphere.2018.05.092

Duval, J.F.L., 2007. Electrophoresis of soft colloids: basic principles and applications, in: Willinson, K.J., Lead, J.R. (Eds.), Environmental Colloids and Particles:Behaviour, Separation and Characterization. John Wiley & Sons, Ltd.

Duval, J.F.L., Slaveykova, V.I., Hosse, M., Buffle, J., Wilkinson, K.J., Jérôme F. L. Duval, *,†,‡, Vera I. Slaveykova, §, Monika Hosse, †, Jacques Buffle, † and, Wilkinsonǁ, K.J., 2006. Electrohydrodynamic properties of succinoglycan as probed by fluorescence correlation spectroscopy, potentiometric titration and capillary electrophoresis. Biomacromolecules 7, 2818–2826. https://doi.org/10.1021/bm060346n

Duval, J.F.L., Wilkinson, K.I., Van Leeuwen, H.P., Buffle, J., 2005. Humic substances are soft and permeable: Evidence from their electrophoretic mobilities. Environ. Sci. Technol. 39, 6435–6445. https://doi.org/10.1021/es050082x

Ferreiro, E.A., Helmy, A.K., De Bussetti, S.G., 1995. Interaction of Fe-oxyhydroxide colloidal particles with montmorillonite. Clay Miner. 30, 195–200. https://doi.org/10.1180/claymin.1995.030.3.03

Gao, J., Mikutta, R., Jansen, B., Guggenberger, G., Vogel, C., Kalbitz, K., 2020. The multilayer model of soil mineral–organic interfaces—a review. J. Plant Nutr. Soil Sci. 183, 27–41. https://doi.org/10.1002/jpln.201900530

Goldberg, S., 1989. Interaction of aluminum and iron oxides and clay minerals and their effect on soil physical properties: A review. Commun. Soil Sci. Plant Anal. https://doi.org/10.1080/00103629009368144

Green-Pedersen, H., Pind, N., 2000. Preparation, characterization, and sorption properties for Ni(II) of iron oxyhydroxide-montmorillonite. Colloids Surfaces A Physicochem. Eng. Asp. 168, 133–145. https://doi.org/10.1016/S0927-7757(00)00448-9

Guénet, H., Davranche, M., Vantelon, D., Gigault, J., Prévost, S., Taché, O., Jaksch, S., Pédrot, M., Dorcet, V., Boutier, A., Jestin, J., 2017. Characterization of iron–organic matter nano-aggregate networks through a combination of SAXS/SANS and XAS analyses: impact on As binding. Environ. Sci. Nano 4, 938–954. https://doi.org/10.1039/C6EN00589F

Hofmann, A., Vantelon, D., Montargès-Pelletier, E., Villain, F., Gardoll, O., Razafitianamaharavo, A., Ghanbaja, J., 2013. Interaction of Fe(III) and Al(III) during hydroxylation by forced hydrolysis: The nature of Al-Fe oxyhydroxy co-precipitates. J. Colloid Interface Sci. 407, 76–88. https://doi.org/10.1016/j.jcis.2013.06.020

Hong, Z., Chen, W., Rong, X., Cai, P., Tan, W., Huang, Q., 2015. Effects of humic acid on adhesion of Bacillus subtilis to phyllosilicates and goethite. Chem. Geol. 416, 19–27. https://doi.org/10.1016/j.chemgeo.2015.10.017

Jellander, R., Marčelja, S., Quirk, J.P., 1988. Attractive double-layer interactions between calcium clay particles. J. Colloid Interface Sci. 126, 194–211. https://doi.org/10.1016/0021-9797(88)90113-0

Ji, Y.Q., Black, L., Weidler, P.G., Janek, M., 2004. Preparation of nanostructured materials by heterocoagulation-interaction of montmorillonite with synthetic hematite particles. Langmuir 20, 9796–9806. https://doi.org/10.1021/la0495579

Jiang, C.L., Séquaris, J.M., Vereecken, H., Klumpp, E., 2012. Effects of inorganic and organic anions on the stability of illite and quartz soil colloids in Na-, Ca- and mixed Na-Ca systems. Colloids Surfaces A Physicochem. Eng. Asp. 415, 134–141. https://doi.org/10.1016/j.colsurfa.2012.10.007

Kleber, M., Sollins, P., Sutton, R., 2007. A conceptual model of organo-mineral interactions in soils: Self-assembly of organic molecular fragments into zonal structures on mineral surfaces. Biogeochemistry 85, 9–24. https://doi.org/10.1007/s10533-007-9103-5

Kloster, N., Avena, M., 2015. Interaction of humic acids with soil minerals: Adsorption and surface aggregation induced by Ca2+. Environ. Chem. 12, 731–738. https://doi.org/10.1071/EN14157

Krause, L., Klumpp, E., Nofz, I., Missong, A., Amelung, W., Siebers, N., 2020. Colloidal iron and organic carbon control soil aggregate formation and stability in arable Luvisols. Geoderma 374, 114421. https://doi.org/10.1016/j.geoderma.2020.114421

Labille, J., 2003. Déstabilisation d'une suspension colloïdale de montmorillonite par coagulation-floculation, en présence de polysaccharides. Institut National Polytechnique de Lorraine.

Labille, J., Thomas, F., Milas, M., Vanhaverbeke, C., 2005. Flocculation of colloidal clay by bacterial

polysaccharides: Effect of macromolecule charge and structure. J. Colloid Interface Sci. 284, 149–156. https://doi.org/10.1016/j.jcis.2004.10.001

Lai, H., Fang, H., Huang, L., He, G., Reible, D., 2018. A review on sediment bioflocculation: Dynamics, influencing factors and modeling. Sci. Total Environ. https://doi.org/10.1016/j.scitotenv.2018.06.101

Laird, D., 2001. Nature of Clay–Humic Complexes in an Agricultural Soil. Soil Sci. Soc. Am. J. 65, 1419. https://doi.org/10.2136/sssaj2001.6551419x

Lartiges, B., El Samrani, A.G., Montargès-Pelletier, E., Bihannic, I., Briois, V., Michot, L., 2019. Aggregating ability of ferric chloride in the presence of phosphate ligand. Water Res. 164, 114960. https://doi.org/10.1016/J.WATRES.2019.114960

Le Meur, M., 2016. Matières en suspension de la Moselle (Lorraine , France) : caractérisation minérale et organique et réactivité vis-à-vis des contaminants métalliques. Université de Lorraine.

Le Meur, M., Mansuy-Huault, L., Lorgeoux, C., Bauer, A., Gley, R., Vantelon, D., Montargès-Pelletier, E., 2017. Spatial and temporal variations of Particulate Organic Matter from Moselle River and tributaries: A multimolecular investigation. Org. Geochem. 110, 45–56. https://doi.org/10.1016/j.orggeochem.2017.04.003

Le Meur, M., Montargès-Pelletier, E., Bauer, A., Gley, R., Migot, S., Barres, O., Delus, C., Villiéras, F., 2016. Characterization of suspended particulate matter in the Moselle River (Lorraine, France): evolution along the course of the river and in different hydrologic regimes. J. Soils Sediments 16, 1625–1642. https://doi.org/10.1007/s11368-015-1335-8

Lin, Z., Li, P., Hou, D., Kuang, Y., Wang, G., 2017. Aggregation mechanism of particles: Effect of Ca2+ and polyacrylamide on coagulation and flocculation of coal slimewater containing illite. Minerals 7. https://doi.org/10.3390/min7020030

Madejová, J., 2003. FTIR techniques in clay mineral studies. Vib. Spectrosc. 31, 1–10. https://doi.org/10.1016/S0924-2031(02)00065-6

Martin, J.R.S., Bihannic, I., Santos, C., Farinha, J.P.S., Demé, B., Leermakers, F.A.M., Pinheiro, J.P., Rotureau, E., Duval, J.F.L., 2015. Structure of Multiresponsive Brush-Decorated Nanoparticles: A Combined Electrokinetic, DLS, and SANS Study. Langmuir 31, 4779–4790. https://doi.org/10.1021/acs.langmuir.5b00530

Mavrocordatos, D., Perret, D., Leppard, G., 2007. Strategies and Advances in the Characterisation of colloids by electron microscopy, in: Wilkinson, K., Lead, J. (Eds.), Environmental Colloids and Particles: Behaviour, Separation and Characterization. John Wiley & Sons, Ltd, Wiley, New York, pp. 345–397.

Mikutta, C., Kretzschmar, R., 2008. Synthetic coprecipitates of exopolysaccharides and ferrihydrite. Part II: Siderophore-promoted dissolution. Geochim. Cosmochim. Acta 72, 1111–1127. https://doi.org/10.1016/j.gca.2007.11.035

Milosevic, M., Berets, S.L., 2002. A review of FT-IR diffuse reflection sampling considerations. Appl. Spectrosc. Rev. 37, 347–364. https://doi.org/10.1081/ASR-120016081

Moon, E.M., Peacock, C.L., 2012. Adsorption of Cu(II) to ferrihydrite and ferrihydrite-bacteria composites: Importance of the carboxyl group for Cu mobility in natural environments. Geochim. Cosmochim. Acta. https://doi.org/10.1016/j.gca.2012.06.012

Mpofu, P., Addai-Mensah, J., Ralston, J., 2004. Flocculation and dewatering behaviour of smectite dispersions: Effect of polymer structure type. Miner. Eng. 17, 411–423. https://doi.org/10.1016/j.mineng.2003.11.010

Nachtegaal, M., Sparks, D.L., 2004. Effect of iron oxide coatings on zinc sorption mechanisms at the clay-mineral/water interface. J. Colloid Interface Sci. 276, 13–23. https://doi.org/10.1016/j.jcis.2004.03.031

Ravel, B., Newville, M., 2005. ATHENA and ARTEMIS: Interactive graphical data analysis using IFEFFIT. Phys. Scr. T T115, 1007–1010. https://doi.org/10.1238/Physica.Topical.115a01007

Reinhardt, A., Wilkinson, K., 2004. Contrasting Roles Of Natural Organic Matter On Colloidal Stabilization And Flocculation In Freshwaters, in: Flocculation in Natural and Engineered Environmental Systems. pp. 143–170. https://doi.org/10.1201/9780203485330.ch7

Rey-Castro, C., Mongin, S., Huidobro, C., David, C., Salvador, J., Garcés, J.L., Galceran, J., Mas, F., Puy, J., 2009. Effective affinity distribution for the binding of metal ions to a generic fulvic acid in natural waters. Environ. Sci. Technol. 43, 7184–7191. https://doi.org/10.1021/es803006p

Schwertmann, U., Cornell, R.M., 1991. Iron oxides in the Laboratory. Preparation and Characterization. Wiley-VCH, Weinheim. https://doi.org/10.1002/9783527613229

Sipos, P., Kis, V.K., Balázs, R., Tóth, A., Kovács, I., Németh, T., 2018. Contribution of individual pure or mixed-phase mineral particles to metal sorption in soils. Geoderma 324, 1–8. https://doi.org/10.1016/j.geoderma.2018.03.008

Sipos, P., Németh, T., Kis, V.K., Mohai, I., 2008. Sorption of copper, zinc and lead on soil mineral phases. Chemosphere 73, 461–469. https://doi.org/10.1016/j.chemosphere.2008.06.046

Sondi, I., Bišćan, J., Pravdić, V., 1996. Electrokinetics of pure clay minerals revisited. J. Colloid Interface Sci. 178, 514–522. https://doi.org/10.1006/jcis.1996.0146

Sowers, T.D., Adhikari, D., Wang, J., Yang, Y., Sparks, D.L., 2018a. Spatial Associations and Chemical Composition of Organic Carbon Sequestered in Fe, Ca, and Organic Carbon Ternary Systems. Environ. Sci. Technol. 52, 6936–6944. https://doi.org/10.1021/acs.est.8b01158

Sowers, T.D., Stuckey, J.W., Sparks, D.L., 2018b. The synergistic effect of calcium on organic carbon sequestration to ferrihydrite. Geochem. Trans. 19, 22–26. https://doi.org/10.1186/s12932-018-0049-4

Tertre, E., Beaucaire, C., Coreau, N., Juery, A., 2009. Modelling Zn(II) sorption onto clayey sediments using a multi-site ion-exchange model. Appl. Geochemistry 24, 1852–1861. https://doi.org/10.1016/j.apgeochem.2009.06.006

Thomas, F., Michot, L.J., Vantelon, D., Montargès, E., Prélot, B., Cruchaudet, M., Delon, J.F., 1999. Layer charge and electrophoretic mobility of smectites, in: Colloids and Surfaces A: Physicochemical and Engineering Aspects. pp. 351–358. https://doi.org/10.1016/S0927-7757(99)00291-5

Totsche, K.U., Amelung, W., Gerzabek, M.H., Guggenberger, G., Klumpp, E., Knief, C., Lehndorff, E., Mikutta, R., Peth, S., Prechtel, A., Ray, N., Kögel-Knabner, I., 2018. Microaggregates in soils. J. Plant Nutr. Soil Sci. https://doi.org/10.1002/jpln.201600451

Town, R.M., Duval, J.F.L., Buffle, J., Van Leeuwen, H.P., 2012. Chemodynamics of metal complexation by natural soft colloids: Cu(II) binding by humic acid. J. Phys. Chem. A 116, 6489–6496. https://doi.org/10.1021/jp212226j

Vindedahl, A.M., Strehlau, J.H., Arnold, W.A., Penn, R.L., 2016. Organic matter and iron oxide nanoparticles: Aggregation, interactions, and reactivity. Environ. Sci. Nano 3, 494–505. https://doi.org/10.1039/c5en00215j

Walling, D.E., 2013. The evolution of sediment source fingerprinting investigations in fluvial systems. J. Soils Sediments 13, 1658–1675. https://doi.org/10.1007/s11368-013-0767-2

Warren, L.A., Zimmermann, A.P., 1994. Suspended particulate grain size dynamics and their implications for trace metal sorption in the Don River. Aquat. Sci. 56, 348–362. https://doi.org/10.1007/BF00877181

Webb, S.W., Stanley, D.A., Scheiner, B.J., 1986. Infrared Examination of Ion-Exchanged Montmorillonite Treated With Polyethylene Oxide. Rep. Investig. - United States, Bur. Mines 9036, 1–16.

Wilkinson, K.J., Lead, J.R., 2007. Environmental Colloids and Particles: Behaviour, Separation and Characterisation, Environmental Colloids and Particles: Behaviour, Separation and Characterisation. https://doi.org/10.1002/9780470024539

Yuan, P., Annabi-Bergaya, F., Tao, Q., Fan, M., Liu, Z., Zhu, J., He, H., Chen, T., 2008. A combined study by XRD, FTIR, TG and HRTEM on the structure of delaminated Fe-intercalated/pillared clay. J. Colloid Interface Sci. 324, 142–149. https://doi.org/10.1016/j.jcis.2008.04.076

FIGURE CAPTIONS

Figure 1: Iron-illite aggregates $IFeH_R$. Size distribution (nm) (red histogram) and electrophoretic mobility μ (m^2 V^{-1} s^{-1} x 10^{-8}) (blue histogram) of illite particles for different initial Fe/illite ratios R = 0.2, 0.6 and 2. (N: number of replicates). Conditions of synthesis: $[Fe(NO_3)_3]$ =10^{-4}M; [KOH] =10^{-3}M; addition rate of iron nitrate: 0.25 mL min^{-1}; addition rate of KOH: 0.1 mL min^{-1}; initial concentration of illite suspension: 200 mg L^{-1}, initial volume of illite suspension 100 mL. The pH of all suspensions analysed after dialysis is 5.7.

Figure 2 : X-ray absorption spectroscopy at Fe-K edge. EXAFS oscillations from Illite (a), IFeH0.6 (b), IFeH2 (c) and FeH (d). The latter sample was synthesized in the same conditions as the others but without illite particles.

Figure 3: High Resolution Transmission Electron Microscopy (HRTEM) images of illite, illite-Fe (hydr)oxide with the ratio iron/illite = 0.2, 0.6 or 2 ($IFeH_{0.2}$, $IFeH_{0.6}$ and $IFeH_2$ respectively) at two magnifications (100k and 200k for illite, 100k and 250k for $IFeH_{0.2}$, $IFeH_{0.6}$ and $IFeH_2$). id: ill-defined edges; nanoFeH: nano iron (hydr)oxide For $IFeH_{0.6}$, the black square indicates the region corresponding to the second picture on the right, obtained at 250k.

Figure 4: Bright Field (BF) and High-Angle Annular Dark-Field (HAADF) scanning transmission electron microscopy (STEM) images of illite-Fe (hydr)oxide with the ratio iron/illite = 0.2, 0.6 or 2 ($IFeH_{0.2}$, $IFeH_{0.6}$ and $IFeH_2$ respectively). ($IFeH_{0.2}$: 2M magnification; $IFeH_{0.6}$ and $IFeH_2$: 1.2M magnification).

Figure 5: Illite-dextran aggregates ID_x. Size distribution (nm) (red histogram) and electrophoretic mobility μ (m^2 V^{-1} s^{-1} x 10^{-8}) (blue histogram) of illite particles for two different initial concentrations of dextran (x = 10 and 100 mg L^{-1} or 1.67 and 16.67 μmol L^{-1}, respectively). (N: number of replicates). Initial concentration of illite suspension: 200 mg L^{-1}, initial volume of illite suspension 50 mL. Initial concentration of $CaCl_2$ = 5.10^{-4} M. The pH of all suspensions analysed after dialysis is 5.7. The green curve represents the electrophoretic mobility of dextran.

Figure 6: Fourier-transform infrared spectra of illite-dextran aggregates ID_x. (above) Transmission mode (Tr) and (below) Diffuse Reflectance mode (DR) spectra: illite (a), dextran (b), illite-dextran aggregates ID_{10} (c) and ID_{100} (d). Spectra have been corrected by the baseline of the device. An adjustment of the signal intensity has been made for their better visualization and qualitative interpretation.

Figure 7: Illite-Fe (hydr)oxide-dextran aggregates. Size distribution (nm) (red histogram) and electrophoretic mobility μ (m^2 V^{-1} s^{-1} x 10^{-8}) (blue histogram) of illite particles for initial Fe/illite ratios R = 0.6 and two different initial concentrations of dextran (1.67 and 16.67 μmol L^{-1}) (N: number of replicates). $[Fe(NO_3)_3]$ =10^{-4}M; [KOH] =10^{-3}M; addition rate of iron nitrate: 0.25 mL min^{-1}; addition rate of KOH: 0.1 mL min^{-1}; initial concentration of illite suspension: 200 mg L^{-1}, initial volume of illite suspension 100 mL. Initial concentration of $CaCl_2$ = 5.10^{-4}M. The pH of all suspensions analysed after dialysis is 5.7. The green line represents the electrophoretic mobility of dextran.

Figure 8: Fourier-Transform Infrared spectra of ternary illite-Fe (hydr)oxide-dextran aggregates $IFeH_RD10$ – Transmission (top graph) and Diffuse Reflectance (bottom graph) spectra of ID_{10} (a), $IFeH_{0.6}D_{10}$ (b), $IFeH_2D_{10}$ (c). Spectra have been corrected by the baseline of the device but are not normalized. An adjustment of the spectrum intensity was performed for a better visualization and qualitative interpretation.

Figure 9: Scheme of the binary illite-dextran (ID_{10}) and ternary illite-Fe (hydr)oxide-dextran ($IFeH_{0.6}D_{10}$ and $IFeH_{0.6}D_{100}$) aggregates. The illite-dextran samples ID_{10} can be represented as large aggregates with a core mainly consituted of clay minerals, floculated by the addition of calcium ions. The large size of this aggregate can be an interpretation key of FTIR data obtained in transmission, suggesting a relatively low content of polymer associated to these aggregates. The seocnd and third schemes presents $IFeH_{0.6}D_{10}$ and $IFeH_{0.6}D_{100}$ samples. Those samples atre represented as smaller aggregates. The presence of nanoFeH on illite surface limited the adsorption of Ca^{2+} on exchangeable cationic sites of clay particles and finally stabilized small size flocs. The presence of the nanoFeH also promoted the adsorption of dextran. The higher concentration of dextran lead to a second population of smaller aggregates.

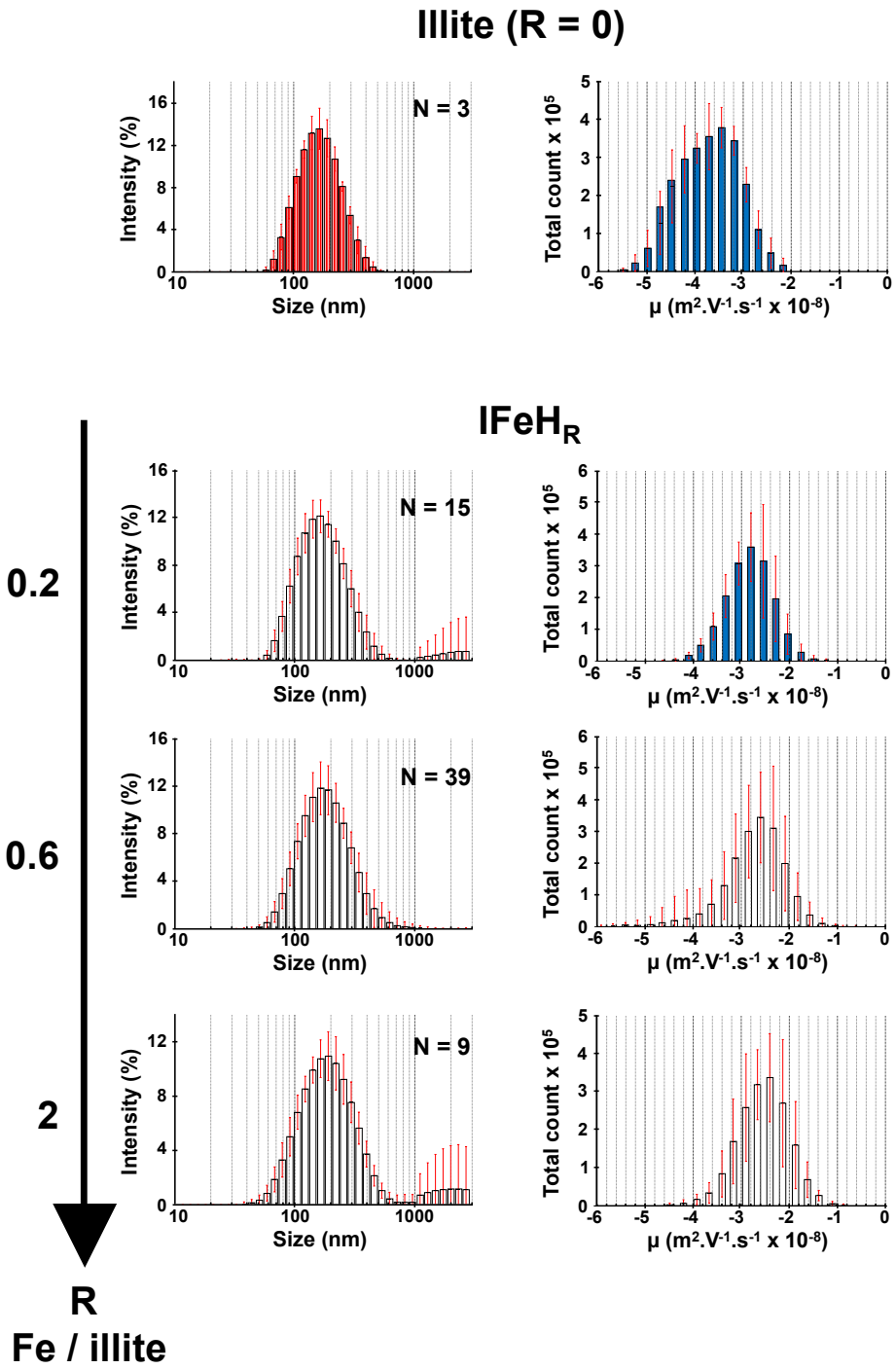

Figure 1: Iron-illite aggregates $IFeH_R$. Size distribution (nm) (red histogram) and electrophoretic mobility μ (m^2 V^{-1} s^{-1} x 10^{-8}) (blue histogram) of illite particles for different initial Fe/illite ratios R = 0.2, 0.6 and 2. (N: number of replicates). Conditions of synthesis: $[Fe(NO_3)_3]$ =10^{-4}M; [KOH] =10^{-3}M; addition rate of iron nitrate: 0.25 mL min^{-1}; addition rate of KOH: 0.1 mL min^{-1}; initial concentration of illite suspension: 200 mg L^{-1}, initial volume of illite suspension 100 mL. The pH of all suspensions analysed after dialysis is 5.7.

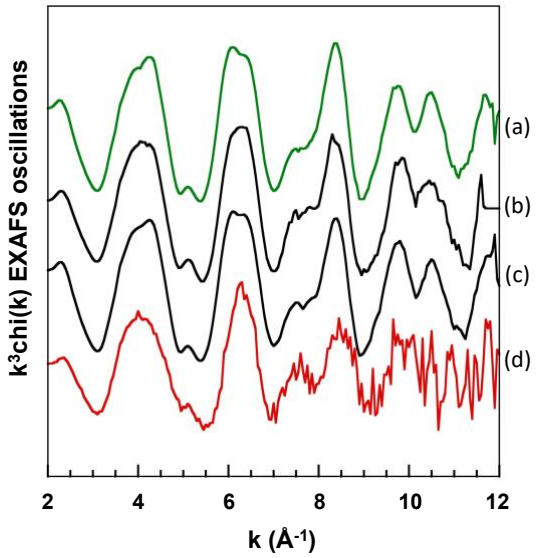

Figure 2: X-ray absorption spectroscopy at Fe-K edge. EXAFS oscillations from Illite (a), IFeH0.6 (b), IFeH2 (c) and FeH (d). The latter sample was synthesized in the same conditions as the others but without illite particles.

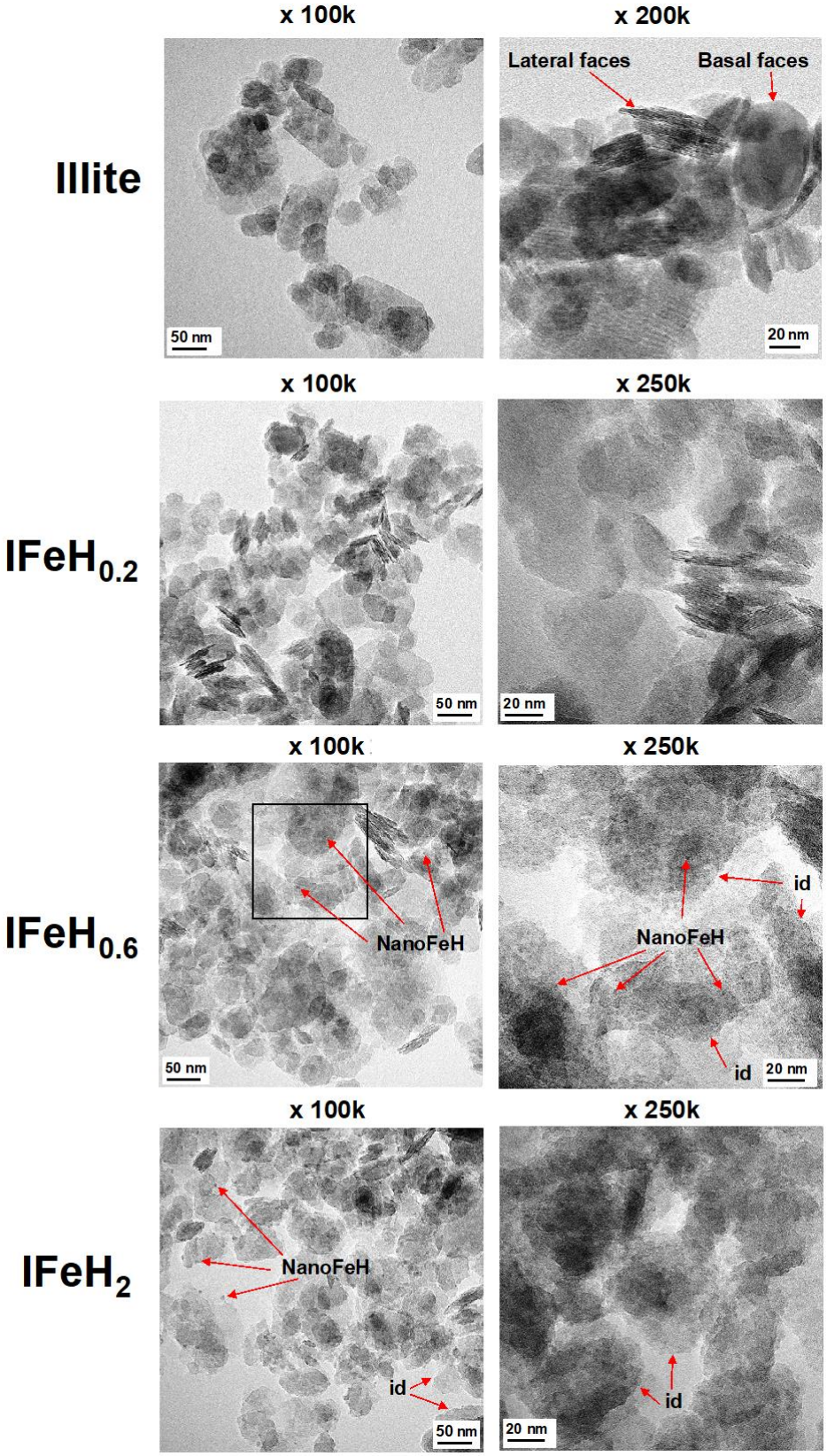

867
868 Figure 3: High Resolution Transmission Electron Microscopy (HRTEM) images of illite, illite-Fe (hydr)oxide with
869 the ratio iron/illite = 0.2, 0.6 or 2 ($IFeH_{0.2}$, $IFeH_{0.6}$ and $IFeH_2$ respectively) at two magnifications (100k and
870 200k for illite, 100k and 250k for $IFeH_{0.2}$, $IFeH_{0.6}$ and $IFeH_2$). id: ill-defined edges; nanoFeH: nano iron
871 (hydr)oxide For $IFeH_{0.6}$, the black square indicates the region corresponding to the second picture on the
872 right, obtained at 250k.
873

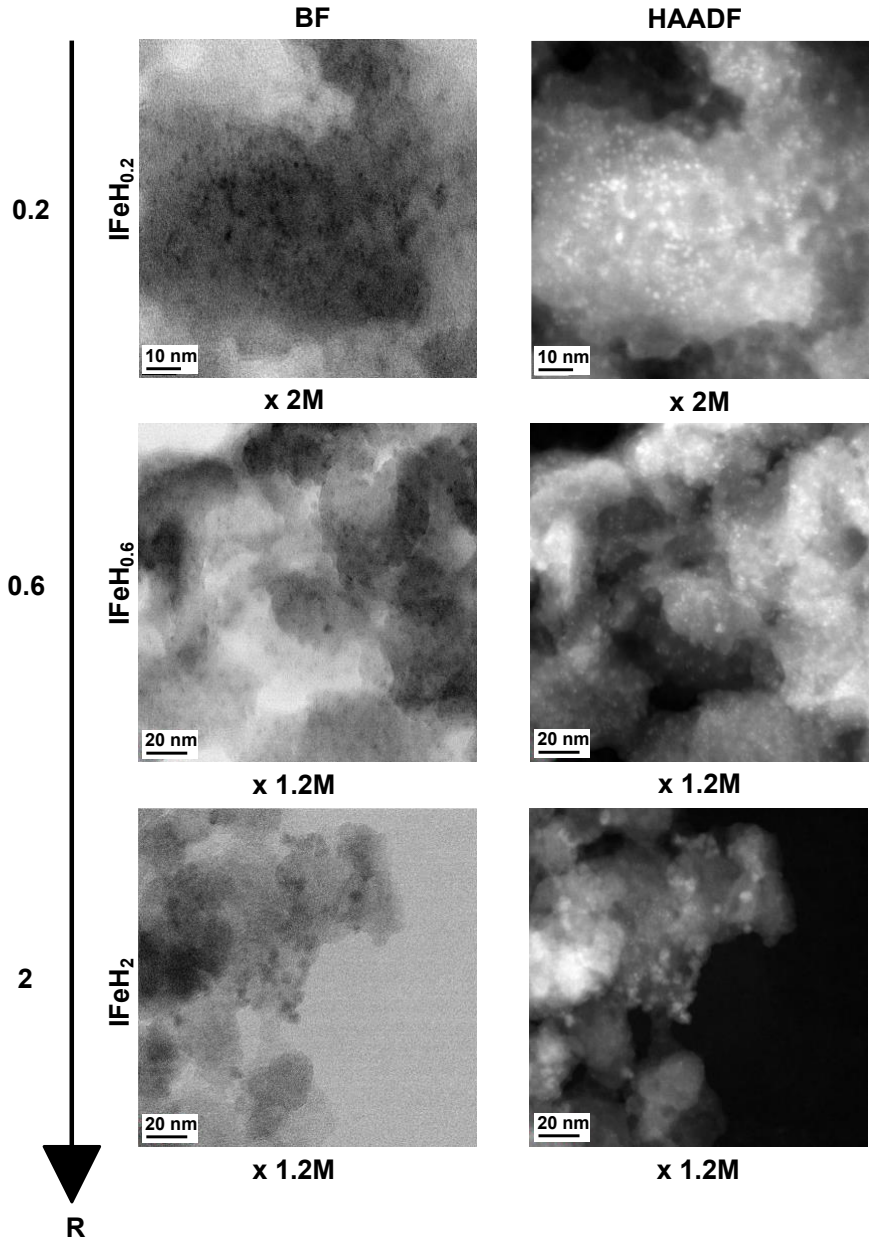

Figure 4: Bright Field (BF) and High-Angle Annular Dark-Field (HAADF) scanning transmission electron microscopy (STEM) images of illite-Fe (hydr)oxide with the ratio iron/illite = 0.2, 0.6 or 2 ($IFeH_{0.2}$, $IFeH_{0.6}$ and $IFeH_2$ respectively). ($IFeH_{0.2}$: 2M magnification; $IFeH_{0.6}$ and $IFeH_2$: 1.2M magnification).

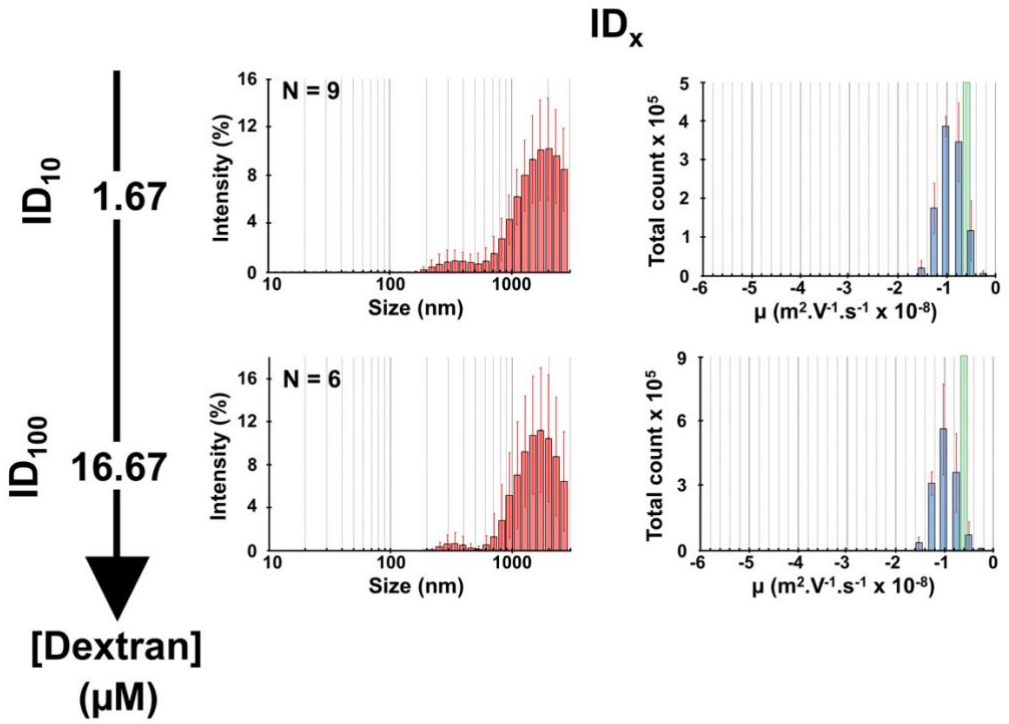

Figure 5: Illite-dextran aggregates ID_x. Size distribution (nm) (red histogram) and electrophoretic mobility µ (m^2 V^{-1} s^{-1} x 10^{-8}) (blue histogram) of illite particles for two different initial concentrations of dextran (x = 10 and 100 mg L^{-1} or 1.67 and 16.67 µmol L^{-1}, respectively). (N: number of replicates). Initial concentration of illite suspension: 200 mg L^{-1}, initial volume of illite suspension 50 mL. Initial concentration of $CaCl_2$ = 5.10^{-4} M. The pH of all suspensions analysed after dialysis is 5.7. The green curve represents the electrophoretic mobility of dextran.

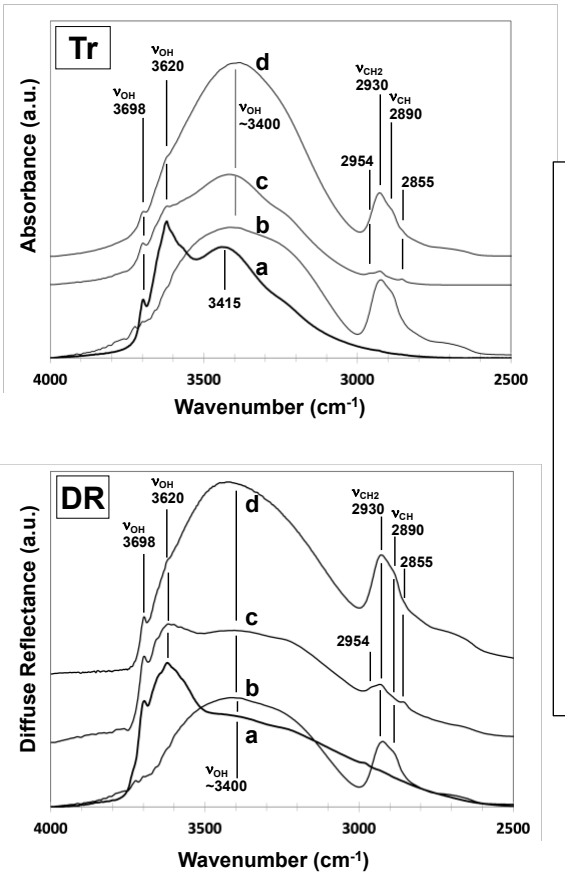

Figure 6: Fourier-transform infrared spectra of illite-dextran aggregates ID_x. (above) Transmission mode (Tr) and (below) Diffuse Reflectance mode (DR) spectra: illite (a), dextran (b), illite-dextran aggregates ID_{10} (c) and ID_{100} (d). Spectra have been corrected by the baseline of the device. An adjustment of the signal intensity has been made for their better visualization and qualitative interpretation.

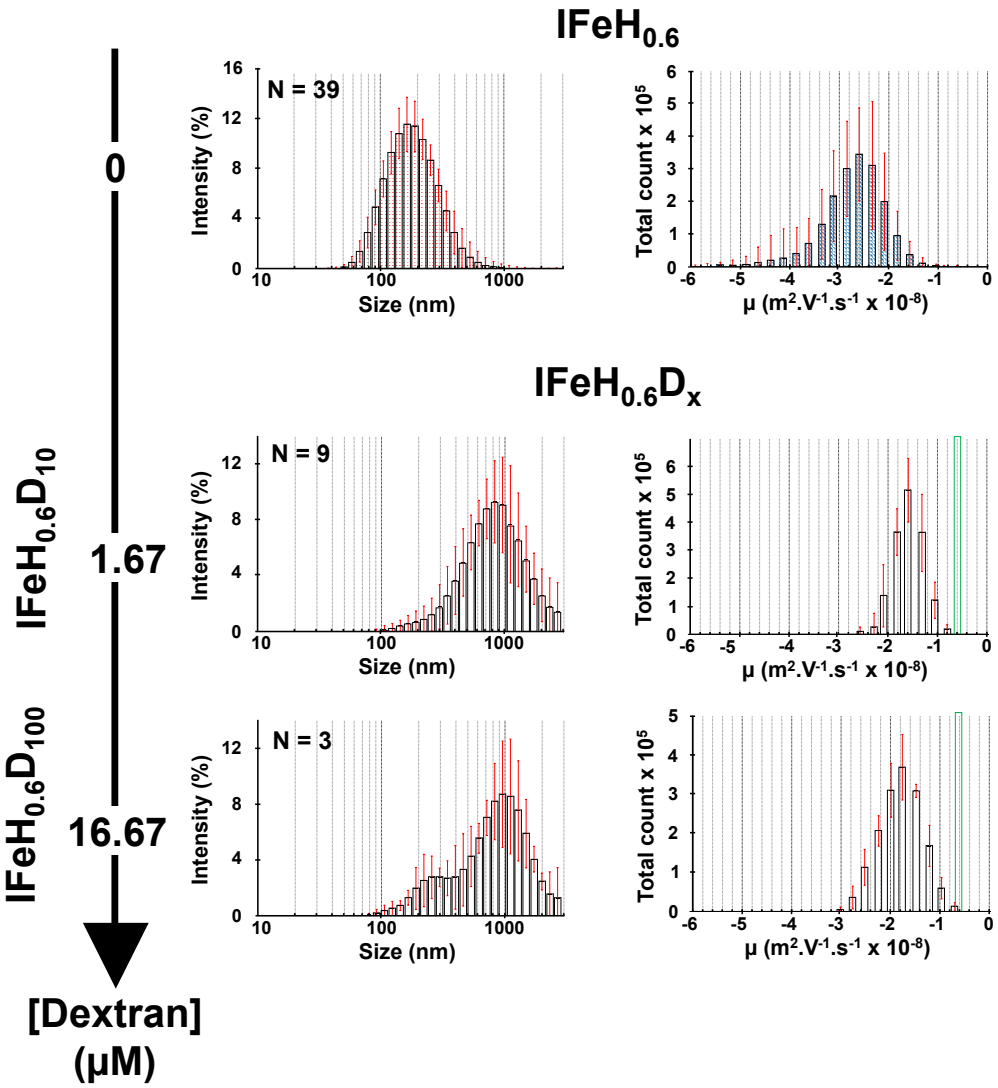

Figure 7: Illite-Fe (hydr)oxide-dextran aggregates. Size distribution (nm) (red histogram) and electrophoretic mobility μ (m^2 V^{-1} s^{-1} x 10^{-8}) (blue histogram) of illite particles for initial Fe/illite ratios R = 0.6 and two different initial concentrations of dextran (1.67 and 16.67 μmol L^{-1}) (N: number of replicates). [$Fe(NO_3)_3$] =10^{-4}M; [KOH] =10^{-3}M; addition rate of iron nitrate: 0.25 mL min^{-1}; addition rate of KOH: 0.1 mL min^{-1}; initial concentration of illite suspension: 200 mg L^{-1}, initial volume of illite suspension 100 mL. Initial concentration of $CaCl_2$ = 5.10^{-4}M. The pH of all suspensions analysed after dialysis is 5.7. The green line represents the electrophoretic mobility of dextran.

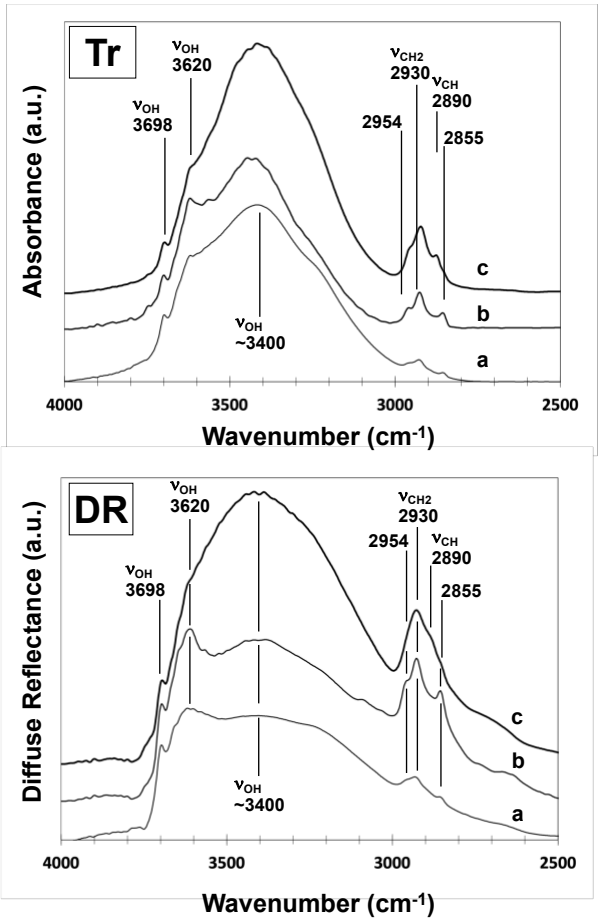

Figure 8: Fourier-Transform Infrared spectra of ternary illite-Fe (hydr)oxide-dextran aggregates $IFeH_RD10$ – Transmission (top graph) and Diffuse Reflectance (bottom graph) spectra of ID_{10} (a), $IFeH_{0.6}D_{10}$ (b), $IFeH_2D_{10}$ (c). Spectra have been corrected by the baseline of the device but are not normalized. An adjustment of the spectrum intensity was performed for a better visualization and qualitative interpretation.

900
901

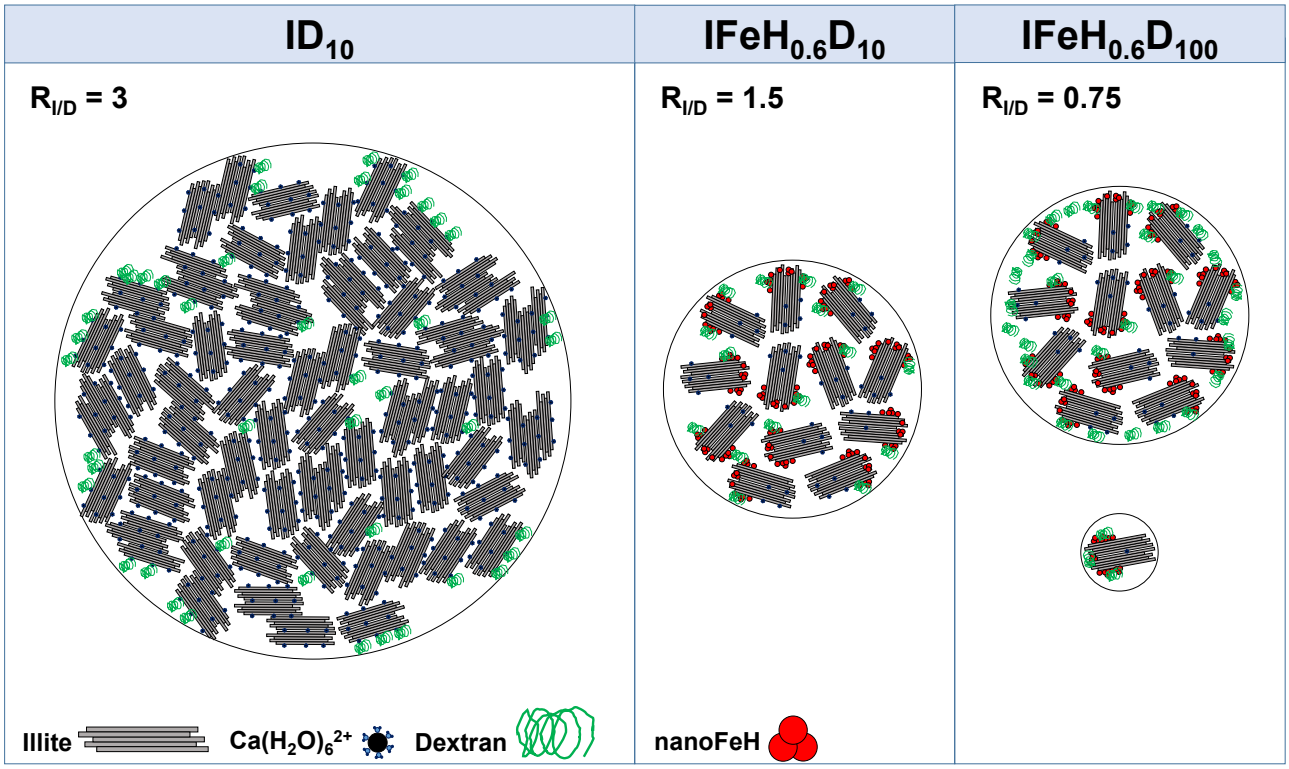

Figure 9: Scheme of the binary illite-dextran (ID_{10}) and ternary illite-Fe (hydr)oxide-dextran ($IFeH_{0.6}D_{10}$ and $IFeH_{0.6}D_{100}$) aggregates. The illite-dextran samples ID_{10} can be represented as large aggregates with a core mainly consituted of clay minerals, floculated by the addition of calcium ions. The large size of this aggregate can be an interpretation key of FTIR data obtained in transmission, suggesting a relatively low content of polymer associated to these aggregates. The seocnd and third schemes presents $IFeH_{0.6}D_{10}$ and $IFeH_{0.6}D_{100}$ samples. Those samples atre represented as smaller aggregates. The presence of nanoFeH on illite surface limited the adsorption of Ca^{2+} on exchangeable cationic sites of clay particles and finally stabilized small size flocs. The presence of the nanoFeH also promoted the adsorption of dextran. The higher concentration of dextran lead to a second population of smaller aggregates.

Supplementary Material 1: Dextran polymer, presentation and properties.

Figure SM-1: (A). Schema of Dextran unit. (B) Electrophoretic mobility μ ($m^2 V^{-1} s^{-1} \times 10^{-8}$) (green histogram) of Dextran, *Dextran concentration 10 mg L^{-1}, $CaCl_2$ concentration 5.10^{-4} M.* ***(C) Fourier-transform infrared spectra of Dextran,*** *transmission mode (Tr) and diffuse reflectance mode (DR) spectra. Spectra have been corrected by the baseline of the device. An adjustment of the signal intensity has been made for their better visualization and qualitative interpretation.*

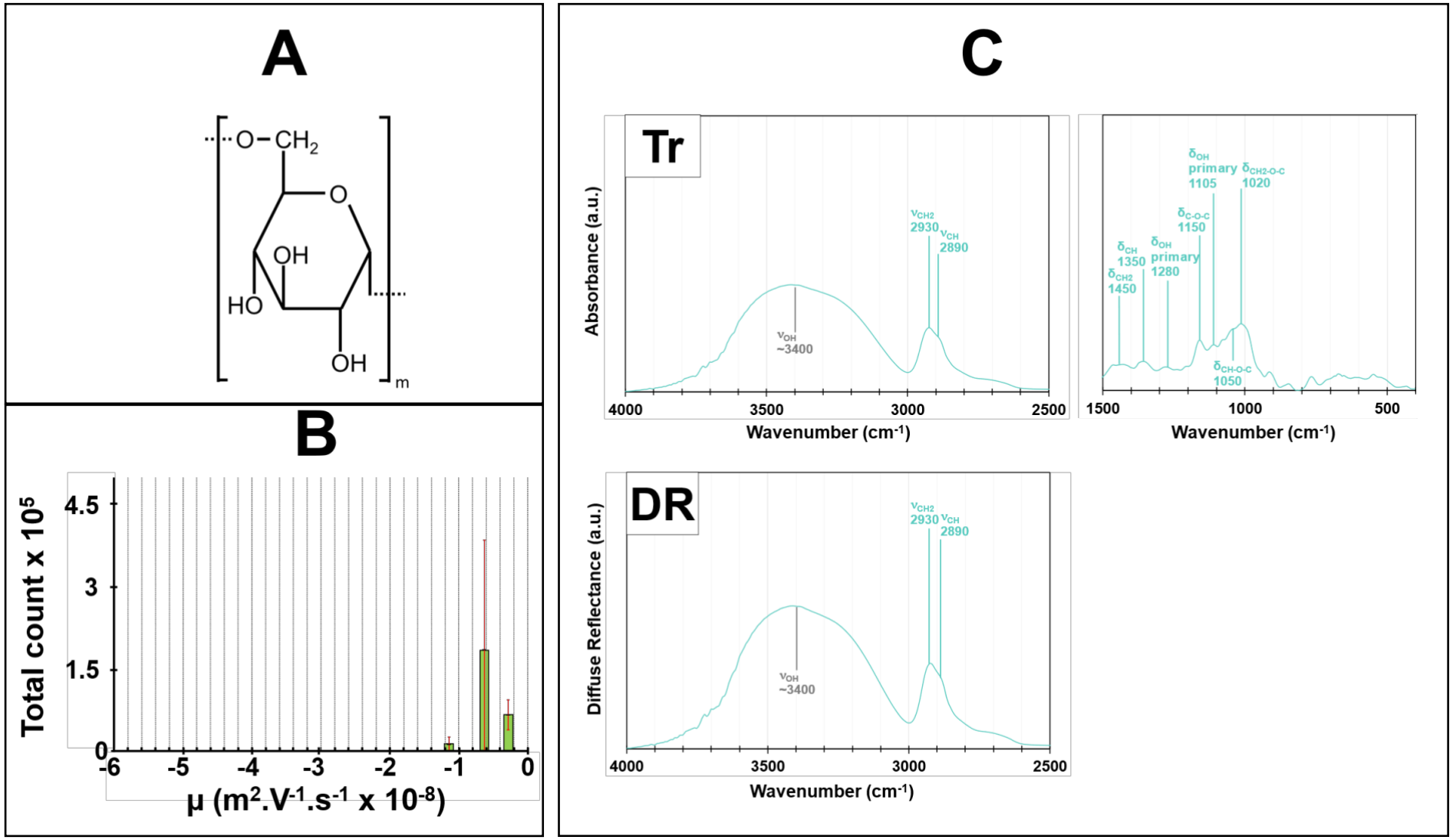

Supplementary Material 2: schematic presentation of the synthesis path of binary and ternary aggregates

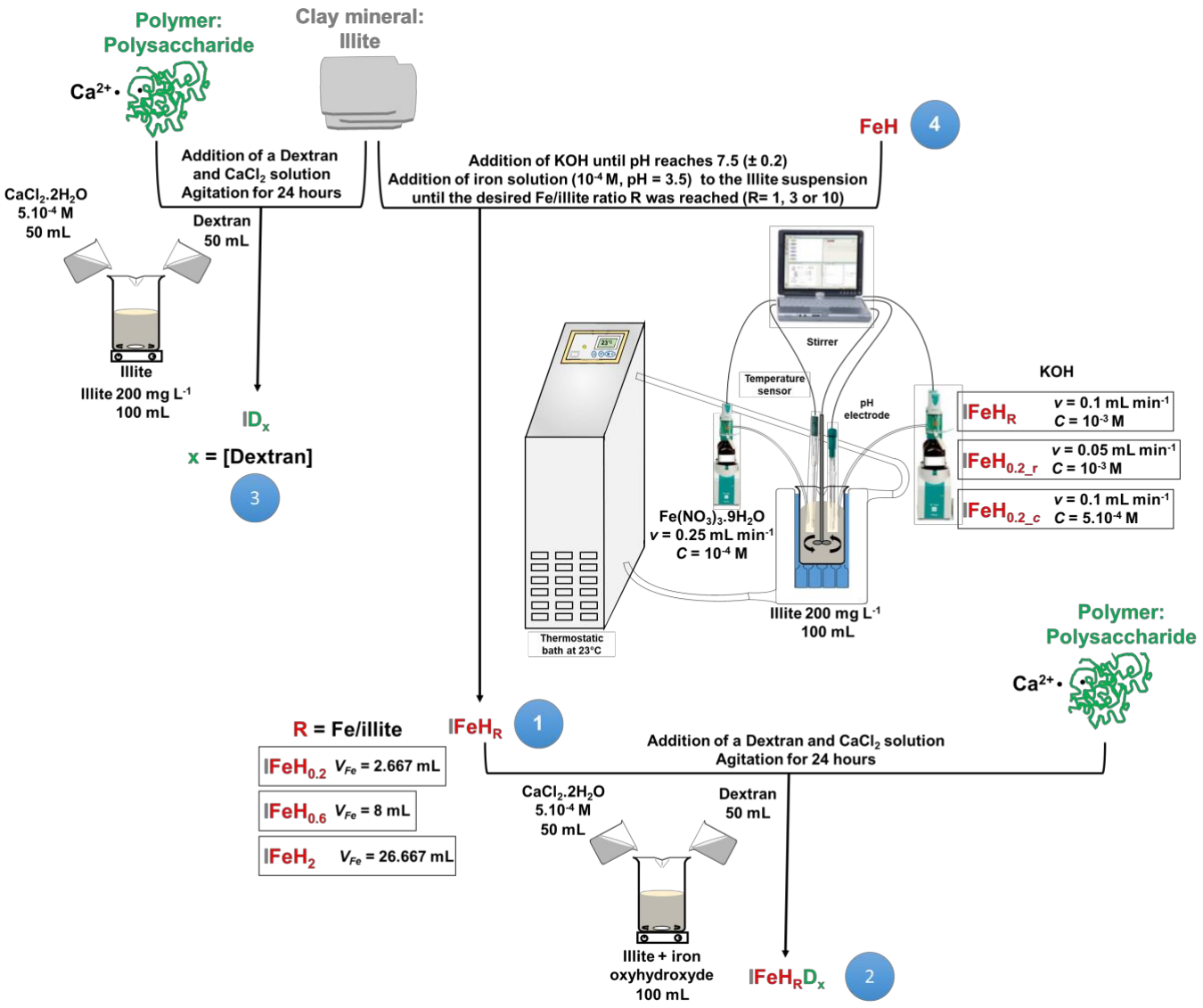

Figure SM-2: *schematic presentation of synthesis protocols*

1-Synthesis of Illite-Fe oxyhydroxide clay-composites IFeH$_R$; iron/illite ratio R, where R = 0.2, 0.6 or 2. The main step of the synthesis of illite-iron oxyhydroxide aggregates is the alkaline hydrolysis of iron salt (iron nitrate) in the presence of illite particles and the resulting products are hereafter differentiated according to initial iron/illite ratio, denoted as R. This ratio was calculated as a function of the CEC value of illite and the amount of iron added to the clay suspension:

$$R = \frac{C_{\mathrm{I\,Fe}}\, V_{\mathrm{Fe\,ad}}}{C_{\mathrm{I}} V_{\mathrm{I}} CEC} \qquad (1)$$

where $C_{\mathrm{i\,Fe}}$ is the concentration of iron nitrate solution (10^{-4} M) and $V_{\mathrm{Fe\,ad}}$ the added volume (2.7, 8 and 27 mL for R = 0.2, 0.6, 2 respectively). C_{I} (200 mg L^{-1}) and V_{I} (100 mL) were the Illite suspension concentration and volume, respectively. CEC (cation exchange capacity) was measured and estimated to 20 meq per 100g of illite.

Experimental conditions were selected to favour the precipitation of iron oxyhydroxide onto the clay mineral surfaces rather than in solution. The $Fe(NO_3)_3$ solution and KOH solution were simultaneously added to the Illite suspension using a Metrohm TITRANDO 809 station. Such a procedure allows reproducible synthesis conditions. Initial clay suspension displays a pH close to 6. Iron solution (10^{-4}M, pH = 3.5) was added to the Illite suspension at a rate of 0.25 mL/min until the desired Fe/illite ratio R was reached (R= 0.2, 0.6 or 2). Simultaneously, KOH was added at a rate of 0.1 mL.min^{-1} until pH reaches 7.5 (± 0.2). Iron nitrate concentration was fixed to 10^{-4} mol L^{-1}, KOH solution was also diluted to slow down hydrolysis kinetics, and the concentration was set to 10^{-3} mol L^{-1}. Such pH and iron concentration conditions were expected to enhance the adsorption of either ferric cations or partially hydrolysed iron species on the cationic exchange sites of illite particles. Titration curves were performed several times (twice for $IFeH_{0.2}$ and $IFeH_2$, nine times for $IFeH_{0.6}$), and display a good reproducibility. Additional experiments were performed at lower KOH concentration (5.10^{-4} mol L^{-1}) or with lower KOH addition rate (0.05 mL min^{-1}) to check the influence of hydrolysis conditions (two supplementary titration curves are presented as supplementary material appendix C). Subsequently, the resulting suspensions were washed to remove salts in excess by dialysis (Spectra/Por® Membrane MWCO 1 kD) until the suspension conductivity was close to that of ultrapure water (<10 µmS.cm^{-1}). All rinsed precipitates were freeze-dried and stored at 20° C prior to analyses.

2-Preparation of aggregates Illite-Iron oxyhydroxide-Dextran referred to as $IFeH_RDx$. The $IFeH_RD_x$ aggregates were prepared by addition of 50 mL of Dextran solution (x =10 or 100 mg L^{-1}) and 50 mL of 5.10^{-4} M $CaCl_2.2H_2O$ solution in $IFeH_R$ suspension. The mixture was stirred for 24 hours and repeatedly dialysed (Spectra/Por® Membrane MWCO 1 kD) until the suspension conductivity was close to that of ultrapure water (<10 µS cm^{-1}). Such a preparation procedure was selected in order to obtain aggregates displaying the three constituents, i.e., illite, iron oxyhydroxides and organic polymer. Indeed, other procedures were tested, and we could observe that when adding Dextran and Calcium solutions to illite suspension prior performing iron hydrolysis, the final products do not present organic polymer in their composition.

3-Preparation of illite-Dextran aggregates (ID_x). A supplementary series of binary samples were prepared to better evidence the influence of iron oxyhydroxides on the interactions between polymer and clay particles. Binary aggregates composed of illite and Dextran polymer were prepared by adding simultaneously 50 mL of Dextran solution (x = 10 or 100 mg L^{-1}, i.e. 1.67 and 16.67 µmol L^{-1} respectively) and 50 mL of $CaCl_2.2H_2O$ solution to the Illite suspension (200mg L^{-1}). The mixture was stirred for 24 hours and repeatedly dialysed (Spectra/Por® Membrane MWCO 1 kD) until the suspension conductivity was close to that of ultrapure water (<10 µS cm^{-1}).

4-FeH was prepared as $IFeH_2$ but without illite particles in the solution. This sample was then compared to $IFeH_R$ samples through XAS spectroscopy**.**

The choice of the different concentrations was based on observations from natural aquatic media. Ca concentrations in continental river waters go from few mg L^{-1} to several 200 mg L^{-1}. 5.10^{-4} M of $CaCl_2$ corresponds to 20 mg L^{-1} for Ca ions. The concentration of illite suspension was set to 100 mg L^{-1} or 200 mg L^{-1}. These concentrations can be compared with solid content in river waters that is few mg L^{-1} in low flow regime and can reach 200 or 300 mg L^{-1} during high flow regime. Dextran concentration and iron (hydr)oxide content were varied and sometimes pushed to high values that were not particularly environmentally relevant, but were used to demonstrate the interactions between the different components.

Supplementary Material 3: Preparation of illite-iron (hydr)oxide clay composites, titration curves.

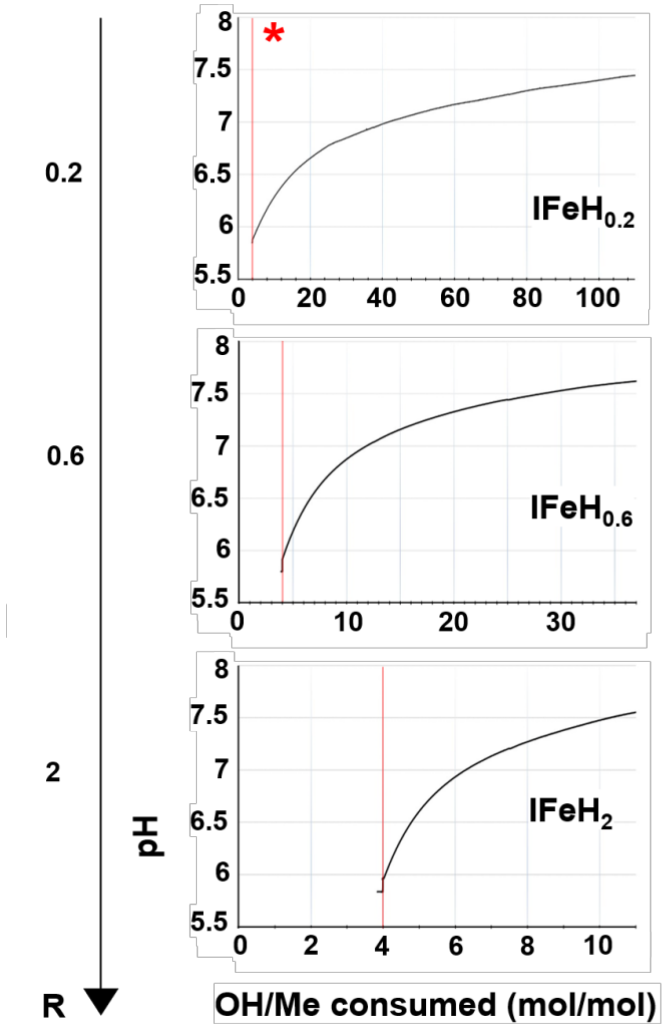

Figure SM-3: pH titration curves for three different initial Fe/illite ratios R = 0.2, 0.6 or 2. *Illite suspension: 200 mg L^{-1}, volume 100 mL. Initial pH value of illite suspension close to 5.7 ± 0.2. Iron concentration in solution, [$Fe(NO_3)_3$] =10^{-4}M, the volume of iron solution was set to 2.7, 8 and 27 mL for the three respective iron/illite ratios. The addition rate of iron nitrate was set to 0.25 mL min^{-1} and the KOH concentration was [KOH] =10^{-3}M, addition rate of KOH: 0.1 mL min^{-1}.*

The formation of binary aggregates $IFeH_R$ (R = 0.2, 0.6 or 2) was monitored via recording the evolution of the pH upon addition of $Fe(NO_3)_3$ and KOH solutions, hereafter denoted as pH titration curves. The first part of the titration curve (before the red line) corresponds to the step of Fe addition. The volume of iron solution to be added is from 2.7 to 27 mL. The higher was R, the higher was the volume of Fe solution to be added, and the longer was the time required for complete addition of Fe. In the first step of the hydrolysis, OH and Fe solution were added simultaneously. During this first step, the pH of the illite suspension slightly increased (from 5.86 to 5.88 for $IFeH_{0.2}$, from 5.8 to 5.92 for $IFeH_{0.6}$ and from 5.84 to 6.05 for $IFeH_2$). This increase in pH suggested that the amount of OH ligands in solution was always sufficient for the hydrolysis of iron cations to occur. As soon as the fixed volume of iron solution was added, there was a clear excess of OH in solution and the pH increased rapidly to c.a. 7.5 for all examined R conditions.

Supplementary Material 4: XANES spectra from IFeH$_R$ samples

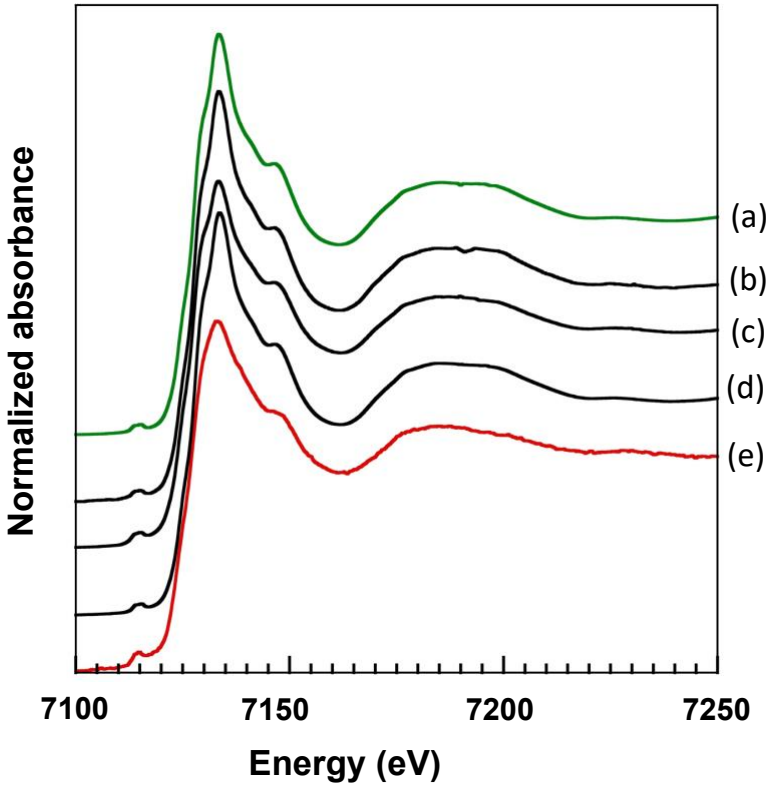

Figure SM-4*: XANES spectra at Fe-K edge and from illite (a), IFeH0.2 (b), IFeH0.6 (c) IFeH2 (d) and FeH (e). The latter sample was synthesized in the same conditions as the others but without illite particles.*

The main absorption peak is relatively sharp for all illite bearing samples (curves a to d), while the FeH spectrum (curve e) displays a rather broad shape. The XANES curves of IFeHR samples are dominated by the signal of iron primarily inserted in the structure of illite (octahedral sheet). The contribution of adsorbed iron (hydr)oxide was not evidenced from these curves and no information about adsorbed iron species could be deduced.

Supplementary Material 5: TEM and HRTEM data on illite-iron oxyhydroxides composites.

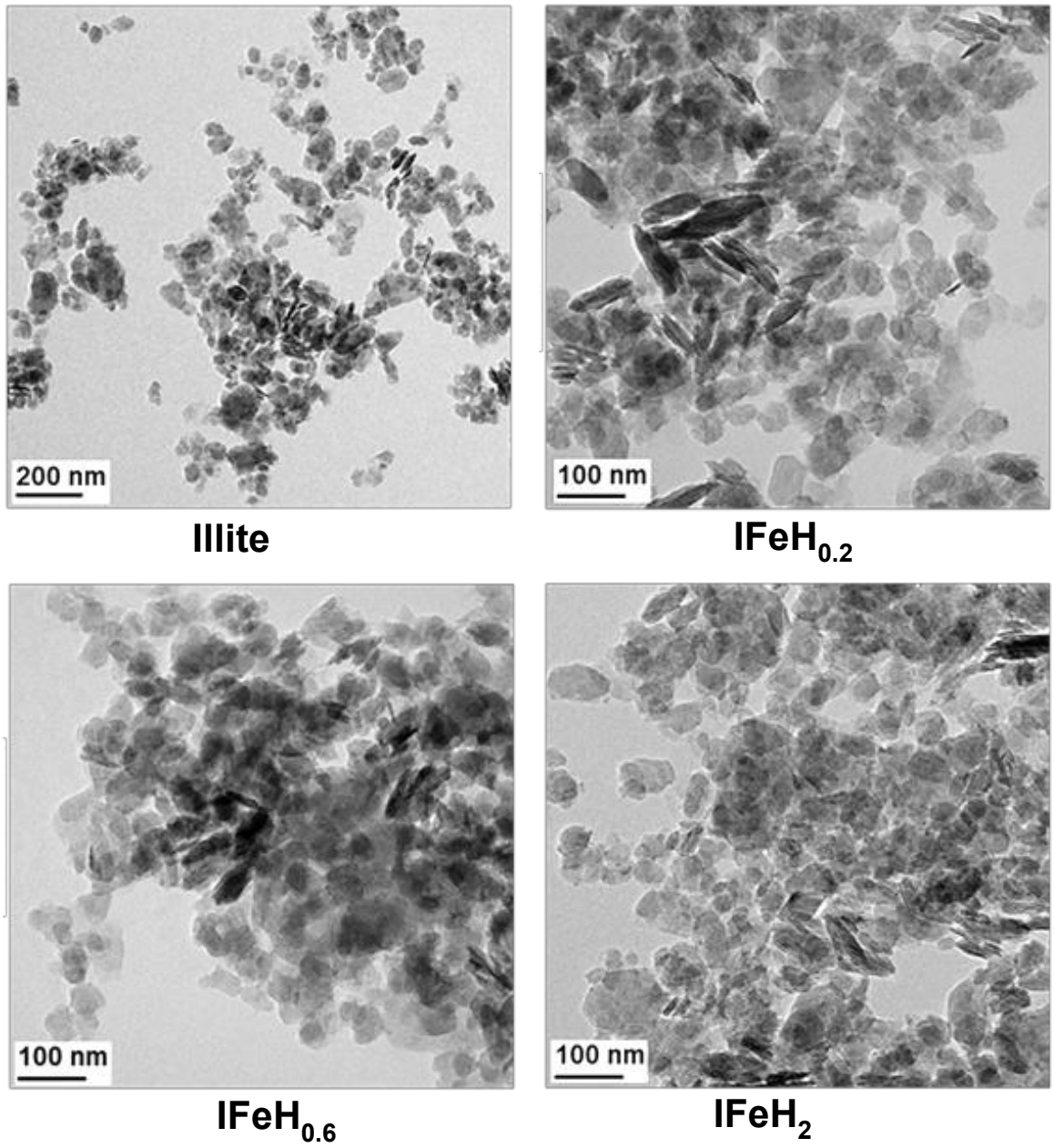

Figure SM-5*:TEM micrographs obtained at low magnification for $IFeH_{0.2}$, $IFeH_{0.6}$ and $IFeH_2$ (30k for Illite, 60k for $IFeH_{0.2}$, $IFeH_{0.6}$ and for $IFeH_2$) of Illite,.*

The TEM micrographs presented above were obtained on the ARM microscope at low magnifications (30 k for illite and 60 k for other samples IFeH0.2, IFeH0.6 and IFeH2). These large fields of view demonstrate the absence of individual micrometric iron (hydr)oxide phases.

EDXS data were collected for two samples on HRTEM microscope using a nanoprobe of few nanometers (2-4 nm). The atomic percentages obtained for the different elements suggest that illite particles contributed to each EDXS spectrum. Furthermore, none of the collected spectra could evidence a large increase of iron atomic percentage. Iron/Silicium atomic ratios were calculated, and those ratios vary slightly within the 0.02-0.21 range. The lower ratios are assigned to bare illite particles.

R		0.2								
Element (%)	O	60.2	59.8	57.3	57.1	57.8	61.6	63.8	60.7	58.3
	Mg	0.3	0.3	0.3	0.6	0.5	0.7	0.4	0.2	0.6
	Al	1.9	2.4	4.2	8.4	7.0	4.3	4.3	0.6	3.3
	Si	32.0	33.2	32.7	27.3	29.3	29.5	29.5	36.3	31.5
	K	0.9	0.5	0.5	0.7	0.4	0.5	0.5	0.8	0.8
	Fe	4.6	3.7	5.0	5.6	4.6	2.5	0.7	0.8	5.2
Fe/Si		**0.14**	**0.11**	**0.15**	**0.21**	**0.16**	**0.08**	**0.02**	**0.02**	**0.17**
R		**0.6**								
Element (%)	O	58.2	57.9	60.5	56.2	59.4	60.4	58.4	61.3	57.6
	Mg	1.9	2.3	3.1	2.6	1.2	2.3	2.8	3.1	0.8
	Al	8.6	7.8	9.0	6.7	11.8	10.6	4.8	7.7	5.6
	Si	25.2	25.7	22.7	24.9	22.7	23.3	28.4	23.4	26.0
	K	0.4	0.3	0.2	0.6	0.3	0.3	0.5	0.3	0.4
	Fe	2.9	1.9	2.4	2.5	1.6	1.5	3.9	2.2	2.6
Fe/Si		**0.12**	**0.08**	**0.11**	**0.10**	**0.07**	**0.06**	**0.14**	**0.10**	**0.10**

Table SM-5*: Energy-Dispersive X-ray Spectroscopy (EDXS)-based elemental analysis expressed in percentage (O: Oxygen, Mg: Magnesium, Al: Aluminium, Si: Silicon, K: Potassium, Fe: iron) and ratio Fe/Si of* $IFeH_{0.2}$ *and* $IFeH_{0.6}$ *(eight analyses each).*

Supplementary material 6: Influence of calcium on illite particle aggregation.

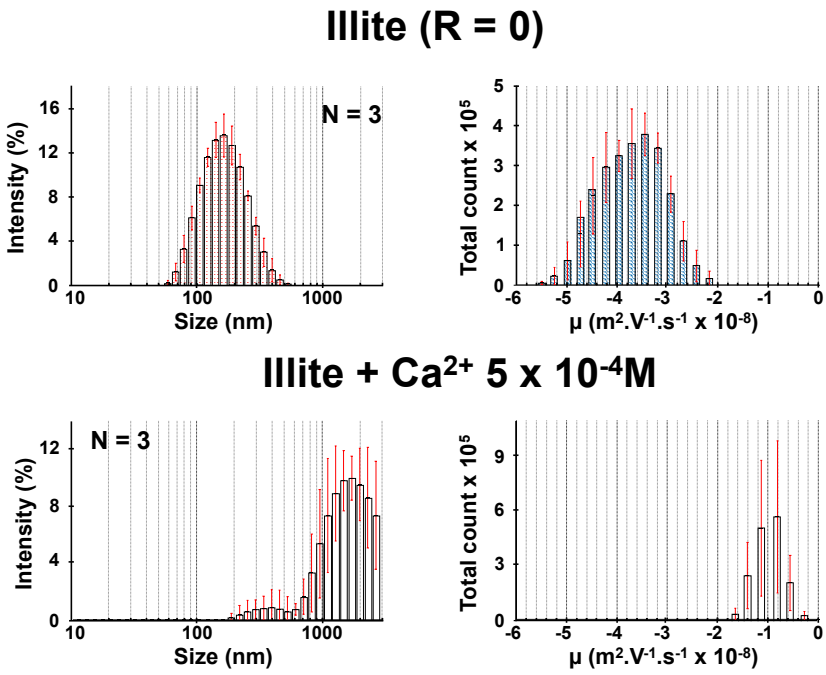

Figure SM-6*: Illite-Ca aggregates. Size distribution (nm) (red curve) and electrophoretic mobility μ (m^2 V^{-1} s^{-1} x 10^{-8}) (blue curve) of illite particles with and without calcium in solution (N: number of replicates). Concentration of illite suspension: 200 mg L^{-1}, initial volume of illite suspension 50mL. Initial concentration of $CaCl_2$ = 5.10^{-4}M.*

$CaCl_2$ addition caused a clear and well-marked increase in particle size distribution (Figure SM-6). The size distribution was shifted towards higher values, with a broad band centred in 1718 μm. Moreover, there was a weak contribution of smaller particles, with a broad band centred at 250 nm. The electrophoretic mobility of illite particles after $CaCl_2$ addition was further shifted towards lesser negative values, with a central value at -1 x 10^{-8} m^2 V^{-1} s^{-1}. The presence of Ca^{2+} in solution screened the repulsive interactions between negatively charged illite particles. Such an electrostatic screening was already reported in numerous publications (Jellander et al., 1988; Jiang et al., 2012; Kloster and Avena, 2015 and references therein).

Supplementary material 7: FTIR spectra of binary and ternary aggregates.

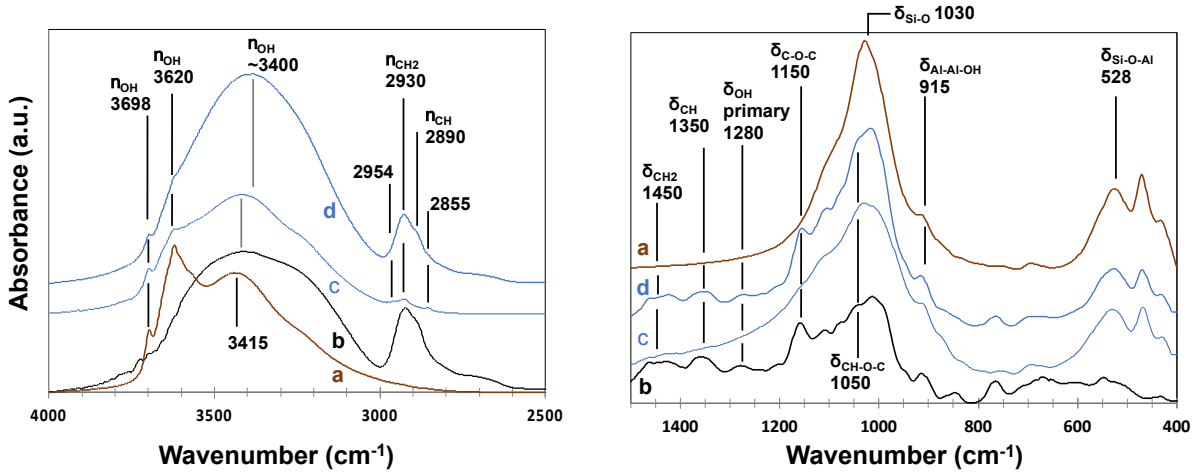

***Figure SM-7A**: Transmission FTIR spectra of IDx aggregates, low wavenumber range. illite (a), dextran (b), illite-dextran aggregates ID_{10} (c) and ID_{100} (d). Spectra have been corrected by the baseline of the device. An adjustment of the signal intensity has been made for their better visualization and qualitative interpretation.*

In transmission mode (Figure SM-7A), the vibration bands of illite (δ_{Si-O} 1030 cm^{-1}, $\delta_{OH-Al-Al}$ 915 cm^{-1}, $\delta_{OH-Al-Fe}$ 886 cm^{-1}, δ_{Si-O} 698 cm^{-1}, $\delta_{OH-Al-Si}$ 528 cm^{-1}) were visible for each of the samples tested and so were the bands corresponding to Dextran (ν_{CH2} 2930 and δ_{CH2} 1450 cm^{-1}, ν_{CH} 2890 and δ_{CH} 1350 cm^{-1}, δ_{OH} 1280 and 1105 cm^{-1}, δ_{C-O-C} 1150 cm^{-1}, $\delta_{CH2-O-C}$ 1050 cm^{-1}, δ_{CH-O-C} 1020 cm^{-1}). The intensity of the bands assigned to Dextran was low for ID_{10} sample and Dextran signature in the 1500-1000 cm^{-1} wavenumber range was hardly detected. With increasing Dextran concentration (ID_{100}), Dextran vibration bands increase in intensity, in line with expectation. Transmission FTIR spectra thus clearly show a strong increase in Dextran content of the formed aggregates from ID_{10} to ID_{100} samples. To quantify the Illite/Dextran ratio, we calculated the ratios of intensity bands respectively centred at 3698 and 2930 cm^{-1}. This ratio decreases from 3.05 to 0.71 for ID_{10} and ID_{100}.

The stretching vibration bands of alkyl groups (ν_{CH2} and ν_{CH}, 3000-2800 cm^{-1}) for pure Dextran are clearly modified for ID_{10} sample. Indeed, for ID_{10}, the contributions of these stretching vibrations are clearly separated whereas pure Dextran displays a broad band centred at 2930 cm^{-1} and a shoulder at 2890 cm^{-1}. Such modifications of Dextran signal likely originate from its interactions with illite surface (through Ca^{2+} bridges). However, for ID_{100} the aforementioned splitting of the ν_{CH} and ν_{CH2} bands is no longer observed, and the Dextran signal is basically similar to that of pure Dextran. This observation was further confirmed upon inspection of the spectra in the low wavenumber range. We concluded that at such high Dextran concentrations, most the polymer chains do not interact with the illite surfaces and that bulk Dextran phase arises in the aggregate.

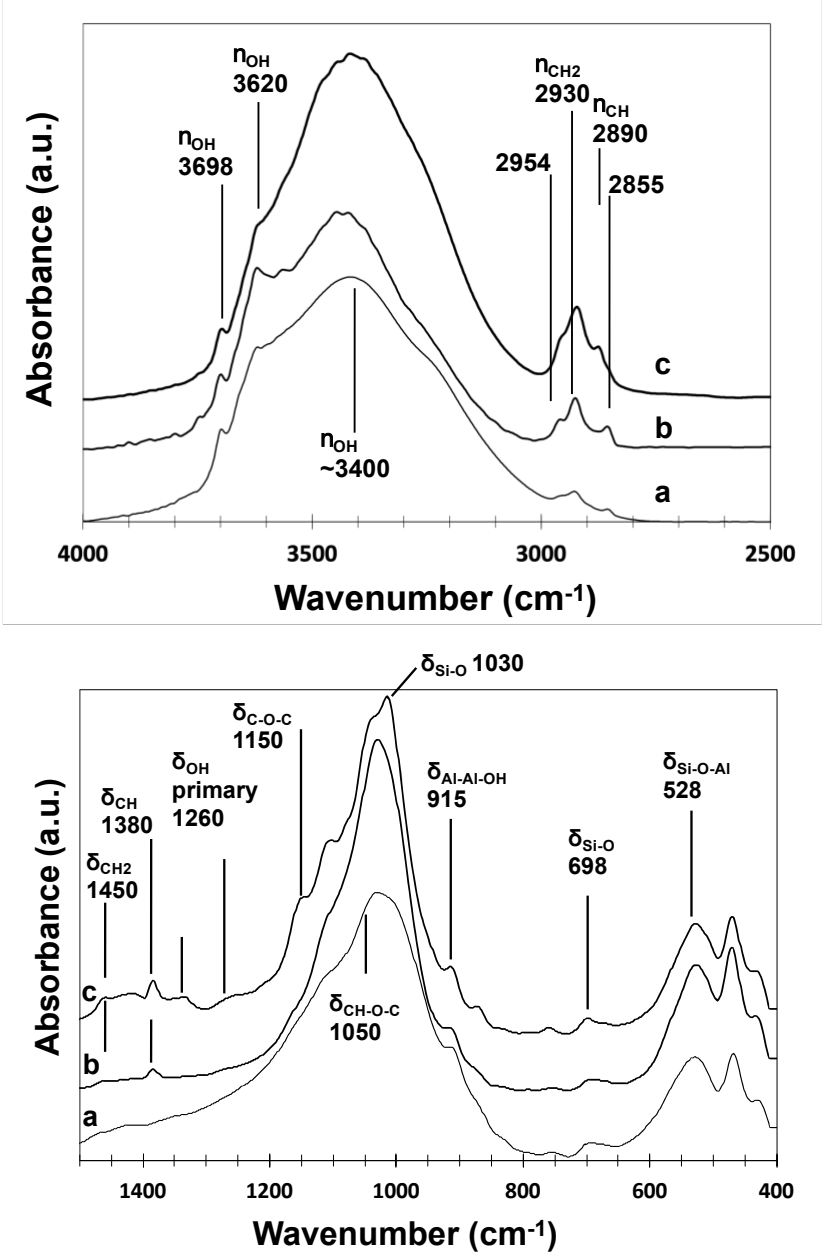

***Figure SM-7B**: Transmission FTIR spectra of ternary illite-Fe (hydr)oxide-dextran aggregates $IFeH_{0.6}D_{10}$ (b), $IFeH_2D_{10}$ (c) and ID_{10} (a. Spectra have been corrected by the baseline of the device but are not normalized. An adjustment (translation) of the signals was performed for a better visualization and qualitative interpretation.*

Figure SM7-B presents the transmission FTIR spectra collected for ID_{10} and $IFeH_RD_{10}$ samples (Figure 9A, top graphs), all prepared with a Dextran concentration set at 10 mg L^{-1}. Those spectra reveal the vibration bands of Illite (ν_{OH} 3698 and 3620 cm^{-1}, $\delta_{Si\text{-}O}$ 1030 cm^{-1}, $\delta_{O\text{-}H\text{-}Al}$ 915 cm^{-1}, $\delta_{OH\text{-}Al\text{-}Fe}$ 886 cm^{-1}, $\delta_{Si\text{-}O}$ 698 cm^{-1}, $\delta_{Si\text{-}O\text{-}Al}$ 528 cm^{-1}) and Dextran in the stretching domain (ν_{CH2} 2930 cm^{-1} and ν_{CH} 2890 cm^{-1}). In the spectral domain corresponding to molecular bending (from 1500 to 1000 cm^{-1}), the presence of Dextran is hardly detected for $IFeH_{0.6}D_{10}$, with a single peak at 1373 cm^{-1} that could be assigned to δ_{CH}. With increasing iron content ($IFeH_2D_{10}$, Figure 9A curve c), the vibration bands of Illite (ν_{OH} 3620 cm^{-1} and $\delta_{Si\text{-}O}$ 1030 cm^{-1}) become less visible while vibration bands of Dextran are more intense. Moreover, the sample $IFeH_2D_{10}$ exhibits a higher amount of water than in $IFeH_{0.6}D_{10}$, as judged by the broad and intense stretching band of OH centred at 3400 cm^{-1}. This higher amount of water Dextran in the sample relates to the higher content of Dextran. For the three samples analysed, the stretching vibration bands of alkyl groups (3000-2800 cm^{-1} range) appear in the form of separated bands, centred at 2954, 2930 and 2890 cm^{-1}. However, the splitting of these signatures is as

pronounced as that identified for $IFeH_{0.6}D_{10}$. To quantify the influence of nanoFeH on Dextran adsorption, intensities ratios were calculated. The intensity ratio I_{3698}/I_{2930} compares the contribution of both illite, and Dextran signal and this ratio decreases from ID_{10} to $IFeH_{0.6}D_{10}$ and $IFeH_2D_{10}$, with the respective values 3.05, 1.49 and 0.77.

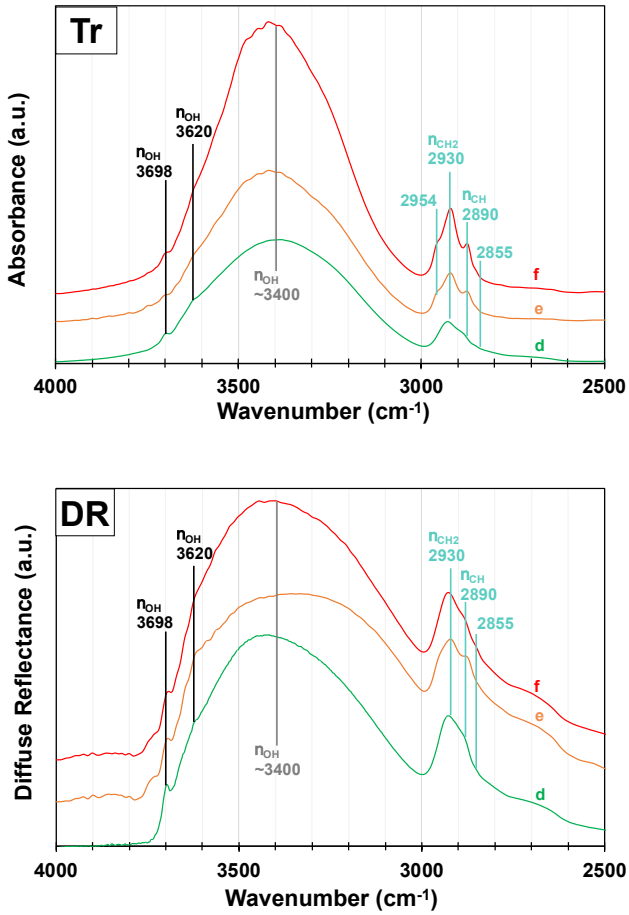

***Figure SM-7C**: Fourier-Transform Infrared spectra of ternary illite-Fe (hydr)oxide-dextran aggregates $IFeH_RD100$ –Transmission (top graph) and Diffuse Reflectance (bottom graph) spectra of ID_{100} (d), $IFeH_{0.6}D_{100}$ (e), $IFeH_2D_{100}$ (f). Spectra have been corrected by the baseline of the device but are not normalized. An adjustment (translation) of the signals was performed for a better visualization and qualitative interpretation.*

Figure SM-7C presents FTIR spectra for the samples prepared with a higher concentration of Dextran (100 mg/L). In transmission mode (top graph), the vibrations of illite OH groups were hardly detected and the intensity ratio I_{3698}/I_{2930} reflecting the respective contributions of illite and Dextran signals basically decreased if compared to that for the previous series of aggregates prepared with 10 mg/L Dextran: this ratio was further slightly decreasing from ID_{100} to $IFeH_{0.6}D_{100}$ and $IFeH_2D_{100}$, with the respective values 0.71, 0.57 and 0.5.

In addition, in transmission mode the vibration bands of Dextran in the stretching region were split for $IFeH_{0.6}D_{100}$ and $IFeH_2D_{100}$,. This splitting demonstrates that OH groups of the polymer are constrained through interactions with illite surface and/or nanoFeH entities. This splitting was not observed for ID_{100} and disappeared in Diffuse Reflectance mode for all $IFeH_RD_{100}$ samples. Moreover, the Diffuse Reflectance spectra evidenced the fading away of illite signal, replaced by Dextran and associated water (bottom graph). At sufficiently high polymer concentrations (100 mg L^{-1}), iron

particles appear to have no influence on the adsorption and on the organization of Dextran within the aggregates, suggesting that the nano-Fe adsorption sites for Dextran are saturated. The above diffuse reflectance observations evidenced that the contribution of illite entities to FTIR signal was significantly screened due to enhanced adsorbed amount of Dextran. These observations also indicated that the higher the Dextran content was, the lower became the fraction of Dextran chains interacting with the mineral surfaces.